AGU PUBLICATIONS

JGR

Journal of Geophysical Research: Solid Earth

RESEARCH ARTICLE
10.1002/2016JB013526

Key Points:
- Imaged a sharp, negative seismic discontinuity pervasively across the Pacific
- There is an age-depth trend beneath young seafloor, flattening at ~60 km depth beneath older ages
- Strength and pervasiveness suggests composition and/or melt at the lithosphere-asthenosphere boundary

Supporting Information:
- Supporting Information S1

Correspondence to:
S. Tharimena,
S.Tharimena@noc.soton.ac.uk

Citation:
Tharimena, S., C. Rychert, N. Harmon, and P. White (2017), Imaging Pacific lithosphere seismic discontinuities—Insights from *SS* precursor modeling, *J. Geophys. Res. Solid Earth*, *122*, 2131–2152, doi:10.1002/2016JB013526.

Received 6 SEP 2016
Accepted 15 FEB 2017
Accepted article online 18 FEB 2017
Published online 11 MAR 2017

Imaging Pacific lithosphere seismic discontinuities—Insights from *SS* precursor modeling

Saikiran Tharimena[1], Catherine Rychert[1], Nicholas Harmon[1], and Paul White[2]

[1]Ocean and Earth Science, University of Southampton, Southampton, UK, [2]Institute of Sound and Vibration Research, University of Southampton, Southampton, UK

Abstract Oceanic lithosphere provides an ideal location to decipher the nature of the lithosphere-asthenosphere system which is vital to our understanding of plate tectonics. It is well established that oceanic lithosphere cools, thickens, and subsides as it ages according to the conductive cooling models. Yet this simple realization fails to explain various observations. For example, old oceanic lithosphere does not subside as predicted. Further, precise imaging of the lower boundary of the oceanic lithosphere has proven challenging. Here we use *SS* precursors to image the discontinuity structure across the Pacific Ocean using 24 years of teleseismic data. We image a sharp pervasive velocity discontinuity (3–15% drop over $<$21 km) at 30–80 km depth that increases in depth with age from the ridge to at least 36 ± 9 Myr along the 1100°C conductive cooling isotherm. Beneath seafloor $>$36 Myr, there is no age-depth dependence, and we image the discontinuity at an average depth of 60 ± 1.5 km. The amplitude and sharpness of the boundary suggests that a compositional variation and/or layered carbonatitic melt may be required to explain our observations rather than temperature alone. The strength and pervasiveness of the boundary suggest that it is likely related to the lithosphere-asthenosphere boundary. An additional deeper discontinuity at 80–120 km depth is imaged intermittently that in most cases likely represents a continuing negative velocity gradient in depth.

1. Introduction

The concept of the lithosphere-asthenosphere system is well defined as the rheological boundary between the rigid lithosphere that transfers coherently and the weaker asthenosphere [*Barrell*, 1914; *Daly*, 1940], but its nature still remains enigmatic since various studies using a variety of geochemical and geophysical techniques have proposed different mechanisms to define the boundary [*Artemieva*, 2006; *Jones et al*., 2001; *Karato*, 2012; *Kawakatsu et al*., 2009; *Moorkamp et al*., 2010; *Regan and Anderson*, 1984; *Rychert and Shearer*, 2011]. Oceanic lithosphere provides an ideal location to understand the nature of the lithosphere-asthenosphere system. To first order, oceanic lithosphere conductively cools resulting in a lithosphere that thickens progressively with age as the plate moves away from the ridge axis, leading to seafloor subsidence. Seismic imaging, heat flow, and gravity studies have shown that seafloor subsides according to half-space cooling (HSC) for oceanic lithosphere $<$70 Myr [*Korenaga*, 2015; *Korenaga and Korenaga*, 2008; *Nishimura and Forsyth*, 1989; *Parsons and Sclater*, 1977; *Stein and Stein*, 1992; *Watts*, 1978]. Yet this simple thermal model fails to explain the shallower than predicted subsidence of old oceanic lithosphere ($>$70 Myr). This apparent deviation from the half-space cooling model has been attributed to additional heat source [*Parsons and Sclater*, 1977; *Smith and Sandwell*, 1997] possibly caused by small-scale convection [*Dumoulin et al*., 2001; *Huang and Zhong*, 2005; *Parsons and Mckenzie*, 1978] and/or hot spot alteration [*Korenaga and Korenaga*, 2008].

The thickness of the oceanic lithosphere likely relates to the observed pattern of seafloor subsidence. Mapping the depth and character of the lithospheric discontinuities, primarily the lithosphere-asthenosphere boundary (LAB), might help to explain observations such as the anomalous subsidence described above. Understanding the nature of the LAB is essential as it has important implications for the driving forces of plate tectonics and mantle convection [*Fischer et al*., 2010]. However, mapping the LAB with existing seismic methods has proven to be a challenge; there is uncertainty on the depth, velocity contrast, and sharpness of the LAB.

In geodynamic modeling, the LAB is placed at the intersection of the geotherm and adiabat that separates the conductively cooled lithosphere from the convecting mantle, classically associated with the depth of the 1300°C isotherm [*Artemieva*, 2006]. In these thermal models the lithosphere thickens with age

following subsidence patterns. The associated predicted seismic velocity gradients from experiments [*Jackson and Faul*, 2010] suggest gradual velocity gradients between the lithosphere and the asthenosphere [*Rychert et al*., 2012]. Plate model (PM) [*Stein and Stein*, 1992] predictions are slightly sharper than half-space cooling (HSC), but seismic velocity gradients are still expected to be very gradual, >80 km for seafloor older than 25 Myr [*Rychert et al*., 2012]. Surface waves also image a lithosphere that thickens with seafloor age over the Pacific Plate in global models [*Maggi et al*., 2006; *Nettles and Dziewonski*, 2008; *Nishimura and Forsyth*, 1989; *Ritzwoller et al*., 2004]. Thickening of the lithosphere has also been observed by using surface waves on a regional scale near the East Pacific Rise [*Harmon et al*., 2009] and beneath the east Pacific Ocean ridges incorporating body waves [*Gu et al*., 2005]. Surface waves offer the most comprehensive map of the oceanic lithosphere velocities although with limited resolution on the sharpness of the LAB transition, which is key to understanding its nature.

A variety of other methods have also been used to constrain the depth and sharpness of oceanic lithospheric discontinuities although with less comprehensive lateral coverage. A receiver function study with a station each on the Pacific Plate and the Philippines Plate observed a sharp (7–8% over 10–15 km) discontinuity with age dependence [*Kawakatsu et al*., 2009; *Kumar and Kawakatsu*, 2011]. *P*-to-*S* receiver functions from stations in the Philippine Sea and northwest Pacific Ocean have been used to infer an age-dependent discontinuity with a gradual velocity change with depth beneath young seafloor, and a sharp constant depth, ~70 km, discontinuity beneath old oceanic crust [*Olugboji et al*., 2016]. Several Pacific transect studies suggest discontinuities at relatively constant depth using a variety of phases; for instance, a sharp negative discontinuity was imaged at 72–112 km depth by using *ScS* phases [*Bagley and Revenaugh*, 2008], at 40–80 km depth by using multiple *S* bounces [*Tan and Helmberger*, 2007], and at 54–64 km depth by using a combination of *ScS* phases, multiple *S* bounces, and surface waves [*Gaherty et al*., 1999]. *SS* precursor studies have also imaged a sharp LAB but one suggesting age dependence [*Rychert and Shearer*, 2011] and the other interpreted as a very subtle age-depth dependence [*Schmerr*, 2012]. These studies suggest that the discontinuities imaged in the 60–110 km depth range beneath the Pacific may not have a simple thermal origin. Mechanisms such as chemical composition [*Gaherty et al*., 1999], hydration [*Hirth and Kohlstedt*, 1996; *Karato*, 2012], anisotropy [*Auer et al*., 2015; *Beghein et al*., 2014], elastically accommodated grain boundary sliding [*Karato*, 2012; *Karato et al*., 2015; *Olugboji et al*., 2016], and/or partial melt [*Kawakatsu et al*., 2009; *Kumar and Kawakatsu*, 2011; *Tan and Helmberger*, 2007] may be required along with temperature to explain these seismic observations of a boundary that does not necessarily follow a simple age-depth trend but could affect and/or define the LAB. These discontinuities may have important implications for our understanding of the LAB and plate tectonics. However, directly connecting these discontinuities to the LAB has proved challenging. A more comprehensive imaging of discontinuity structure at high resolution is required over an entire oceanic plate to better understand the nature, evolution, and defining mechanism of the lithosphere-asthenosphere system.

In this study, we focus on seismically imaging the Pacific lithosphere using *SS* precursors, which are sensitive to the structure near the bounce points (Figure 1). We comprehensively image the discontinuity structure across most of the Pacific at a high resolution. We test for multiple discontinuities including positive discontinuities and provide a detailed view of the depth and pervasiveness of discontinuities across the Pacific. Finally, we discuss possible anisotropic contributions to observed discontinuities.

2. Methods

We build on the *SS* Lithospheric Profiling method of *Rychert and Shearer* [2011] (hereafter referred to as RS11) to image lithospheric discontinuities beneath the Pacific. The *SS* seismic phase is an *S* wave that bounces once at the surface of the Earth before arriving at a station (Figure 1). *SS* precursors are underside reflections from velocity discontinuities that arrive before the main *SS* phase due to shorter paths through the upper mantle. *SS* precursors are sensitive to the discontinuity structure near the bounce point, which is halfway between the source and the receiver (Figure 1a). The advantage of using *SS* waveforms is that it allows us to image the lithospheric structure beneath regions that have sparse station coverage. These precursors are generally weak and cannot be consistently identified on individual seismograms. However, multiple seismograms can be stacked to bring these features above the noise [*Shearer*, 1991b; *Shearer et al*., 1999]. *SS* precursors have been traditionally used to image deeper discontinuities such as the 410, 520, and

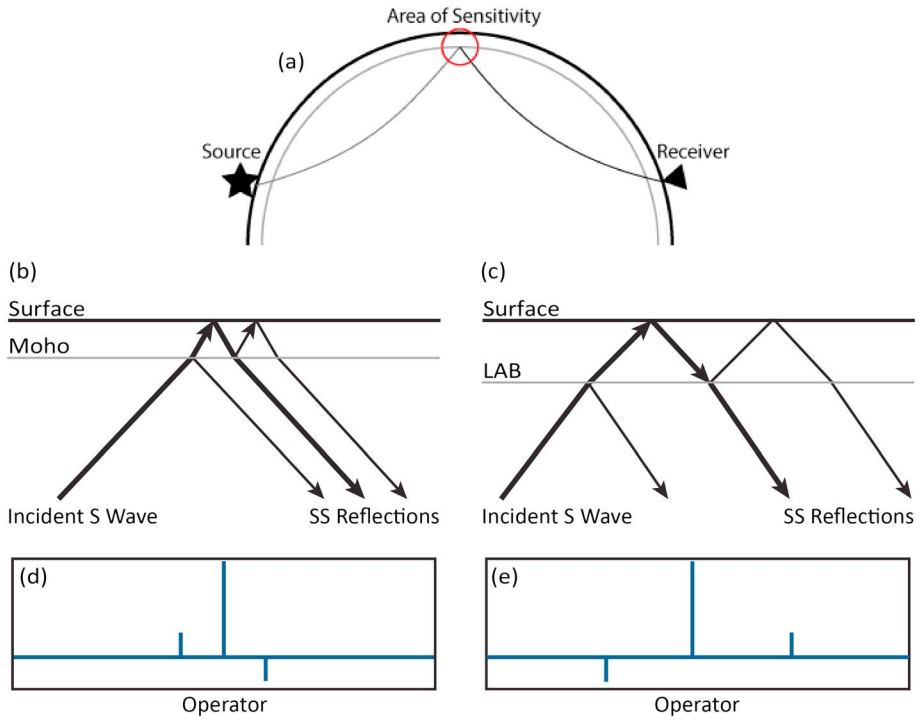

Figure 1. (a) Schematic showing *SS* bounce point sampling remote location located halfway between the source and the receiver. Raypaths of the *SS* waveform (bold), the *SS* precursor, and reverberation are shown for (b) a velocity increase with depth and (c) a velocity decrease with depth. (d and e) Lithospheric operators corresponding to velocity structures shown in Figures 1b and 1c, respectively.

660 km discontinuities [*Chambers et al*., 2005; *Deuss*, 2009; *Deuss and Woodhouse*, 2002; *Flanagan and Shearer*, 1998; *Gu and Dziewonski*, 2002; *Houser et al*., 2008; *Lawrence and Shearer*, 2008; *Niu et al*., 2002; *Shearer*, 1991b, 1993, 1996; *Shearer and Masters*, 1992]. *SS* precursors have also been used to image shallow discontinuity structure such as the Moho across Asia [*Heit et al*., 2010; *Rychert and Shearer*, 2010] and lithospheric discontinuities beneath the Pacific [*Rychert and Shearer*, 2011; *Schmerr*, 2012; *Tharimena et al*., 2016].

We model stacked *SS* waveforms in a two-stage process. In the first stage, we model the attenuation of the *SS* waveform stack to generate an attenuated reference stack. Then we model the waveform by convolving lithospheric operators corresponding to velocity discontinuity structure with the attenuated reference stack.

2.1. Data and Stacking

We used the Incorporated Research Institutions for Seismology (IRIS) data set from 1990 to 2014 with event to station (epicentral) distances of 90°–180° (Figure S1 in the supporting information). The waveforms were preprocessed to remove instrument response. Events with magnitude >5.5 M_w and source depth <75 km were used to ensure good signal-to-noise ratio and minimize complications arising from depth phases [*Rychert and Shearer*, 2011]. The horizontal components were rotated to radial and transverse components. We considered the transverse components, Hilbert transforming them to produce symmetric pulses. The waveforms were resampled to 10 samples per second and were low-pass filtered at 0.1 Hz. An automated procedure was used to eliminate seismograms with incomplete records. The *SS* phase was picked as the maximum amplitude (positive or negative), in a time window 40 s before and after the theoretical *SS* arrival time. The amplitude of each seismogram was normalized to the *SS* phase. The waveforms were centered on the *SS* phase, and records with negative amplitude were flipped to align with the maximum positive amplitude. Each record was then weighted to its signal-to-noise ratio, which is the ratio of the maximum *SS* amplitude to the standard deviation in a time window 270 s to 30 s preceding the *SS* pulse. Waveforms with signal-to-noise ratio <4 were rejected. Additionally, waveforms with normalized amplitudes >1 within a 90 s window preceding the *SS* pulse and/or long period noise evaluated as zero-crossing of *SS* pulse >20 s were also rejected. We obtained 999,593 waveforms with bounce points beneath the Pacific

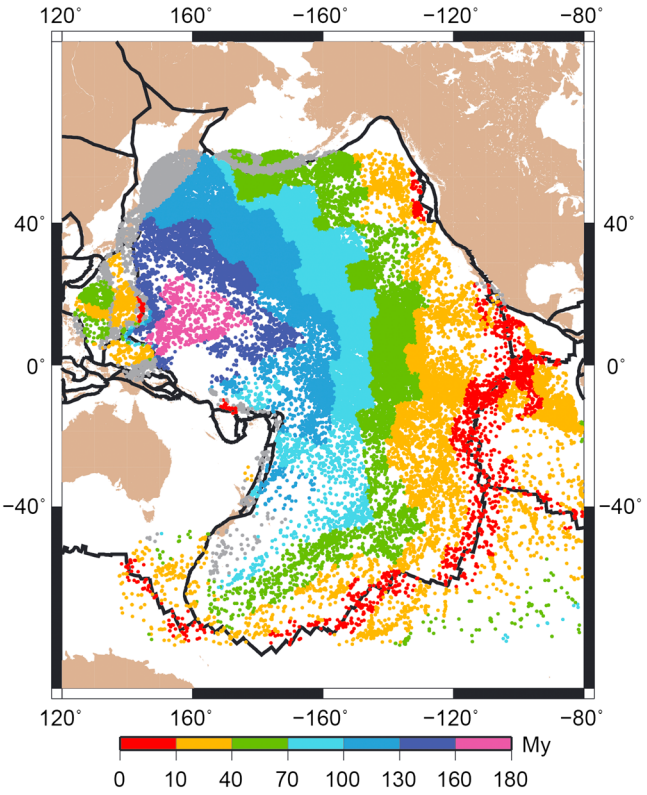

Figure 2. *SS* bounce points used in the 10° Pacific bins. Colors represent seafloor age [*Müller et al.*, 2013]. The grey dots are bounce points with no age estimate. The solid black lines represent plate boundaries [*Bird*, 2003].

that fit the source parameters described above, 89,478 of which also fit the signal-to-noise, *SS* peak, and long-period noise criteria (Figure 2). The waveforms were then aligned on the maximum amplitude, stacked, and normalized to unit amplitude.

2.2. Pacific Binning

We divided the Pacific Ocean into 10° bins, spaced about 10° apart, which approximates the Fresnel zone of the *SS* phase at long periods (Figure S2) [*Shearer*, 1991a; *Tharimena et al.*, 2016]. Our event-station distribution results in an ~10° region of sensitivity centered on our bins (Figure S2), thereby limiting the effect of off-axis structures due to the saddle-shaped Fresnel zone of individual *SS* bounce points [*Deuss and Woodhouse*, 2002; *Shearer*, 1991a; *Tharimena et al.*, 2016]. Waveforms with bounce points (Figure 2) within the 10° bins were stacked by using the procedure described in the previous section. Although the majority of bins have >500 waveforms, bins in the South Pacific generally have <500 waveforms. Unlike the method of RS11, we do not restrict the inversion to bins with >500 waveforms. This was possible since we imposed additional quality control checks on the data while stacking. The quality checks included rejecting waveforms with long-period noise, precursor energy greater than the main *SS* pulse, and indiscernible *SS* pulses by visual inspection. These stringent standards ensured that only good quality seismograms were included in the stack. Visual inspection of the stacks indicated that at least 150 waveforms are required to be well resolved from the best fitting attenuated waveform, and noise degrades the quality of stacks with <150 waveforms, for which the SNR < 4 (Figure S3).

Errors in the data bin were estimated by using bootstrap resampling with replacement. We stack the same number of *SS* waveforms in each bin, but randomly resampling them from the original stack of each bin allowing repetition of waveforms. We perform 100 bootstraps for each bin.

2.3. Pacific Bin Attributes

The age of bins is calculated as a weighted average of the age of bounce points included in the bin determined by a spatially filtered grid from the model of *Müller et al.* [2013]. We classify bounce points in each bin as "normal" (simple history) or "anomalous" (altered) based on the correlation criteria model of *Korenaga and Korenaga* [2008]. We then use the weighted average of these bounce points to classify each bin as normal or anomalous using a 50:50 cutoff.

2.4. Reference Phase

The reference phase is composed of an *S* wave stack convolved with an attenuation operator, *t**. The inversion for *t** is performed first before continuing on to the inversion for discontinuity structure. ***t**** was allowed to vary from 3 to 6 s in the inversions [*Bhattacharyya et al.*, 1996]. The ***t**** operator primarily affects the width of the main *SS* pulse [*Rychert and Shearer*, 2011] and does not interfere with the precursors (Figure S4). Therefore, small variation in the attenuation operator do not significantly affect the depth or sharpness of the discontinuities in our final results. The *S* waveform stacks are produced by using a similar

procedure to that used for *SS* as described in section 2.1. We use data within epicentral distances of 30°–55°. The same magnitude and depth cutoffs applied to *SS* waveforms were applied. Waveforms are weighted to their signal-to-noise ratio. We tested two reference phases. The first reference phase is for the Pacific Ocean computed by using all the *S* waveforms, and the second is a set of *S* reference stacks computed for each 10° bin using the same sources included in the corresponding *SS* stack. There was no significant difference in our results using either the Pacific *S* or bin-specific *S* reference waveforms. In all cases the difference in the depth estimates is $< \pm 4$ km and the amplitude is $< \pm 1\%$. For simplicity we show results using the bin-specific *S* reference waveform in our study. For the bin-specific *S* reference stacks, the signal-to-noise ratio is scaled such that the total weight of an event (in the *SS* stack) is preserved in the *S* stacks. This eliminates possible bias from source effects that might be specific to a particular bounce point bin [*Rychert and Shearer*, 2011]. The reference phase also includes a 7 km thick oceanic crust with a crustal velocity of 3.75 km/s and Moho reflection coefficient of 0.05.

We tested the effect of varying crustal thickness on our inversions. We used CRUST1.0 [*Laske et al*., 2012] to calculate average crustal thickness for each bin. Crustal thickness of bins varies from 6.9 km to 11.2 km with an average crustal thickness of 7.2 km across the Pacific. Only a couple of bins in the far northwest Pacific have crustal thickness of 10.1 km and 11.2 km. Our tests showed negligible effect of variable crustal operator on our inversions, and hence, we chose a constant crustal thickness of 7 km.

2.5. Modeling

We model the stacked data waveform from 0 to 300 s preceding the *SS* arrival, searching for discontinuities in the ~20–200 km depth range. Our synthetic waveforms are computed by convolving the attenuated reference waveform with a lithospheric operator corresponding to the discontinuity. We allowed the time-offset of the operator to vary, to model discontinuities at a variety of depths. We allowed a range of amplitudes to model a range of velocity contrasts. We allowed both positive (velocity increase with depth) and negative (velocity decrease with depth) discontinuities in our models. An example of a positive discontinuity is the Moho (Figures 1b and 1d), and a negative discontinuity is the LAB (Figures 1c and 1e). We use a Gaussian function to investigate a range of discontinuity sharpnesses, i.e., step functions to gradual velocity changes [*Rychert and Shearer*, 2011; *Tharimena et al*., 2016]. We first searched for a single discontinuity. Bins that could not be resolved with a single discontinuity were then tested for double discontinuities, again either positive or negative polarity. Adding a second discontinuity to the bins that were well-fit by a single discontinuity did not give a significantly better fit. In the double discontinuity bins, we also allowed for irregularly shaped operators to test our resolution to multiple discontinuities versus gradational velocity contrasts.

We used a differential evolution algorithm [*Price et al*., 2005; *Storn and Price*, 1997] to find the operator(s) that gives the best fit synthetic from 0 to 300 s prior to the main *SS* phase. This approach minimizes both the model storage size and computation time in comparison to a typical grid search (e.g., RS11). In this approach, an initial set (P—parent) of lithospheric operators were chosen. These operators were convolved with a reference waveform, and the goodness-of-fit of the corresponding synthetics was measured. A new set of lithospheric operators (M—mutants) were generated by using a scaled difference of two randomly selected lithospheric operators from the initial set (P) and adding the difference to a third randomly selected lithospheric operator from the initial set (P). The goodness-of-fit of the synthetics using this second set (M) of lithospheric operators was measured. A pairwise comparison of the goodness-of-fit between the initial set (P) and the second set (M) was done to choose the operators from either set P or set M that gave a better fit. This new set of lithospheric operators (N—daughter) became the initial set (P) for the second generation/iteration. The process of generating a mutant set (M) and pairwise comparison set (N) continued until an optimum solution was found. This population based numerical optimizer is similar to the grid search method used by RS11 but allowed for testing multiple discontinuities without an exponential increase in computational time. The benefits of the differential evolution algorithm over grid search for a large number of parameters are well documented [*Price et al*., 2005].

An automated procedure determines the best fitting model parameters by using the differential evolution algorithm for each bootstrap sample in a bin. The error reported in the model parameters corresponds to the range of model parameters within the bootstrapped limits of the data. The error is determined by 95% confidence bounds, which corresponds to two standard deviations of the mean of the resulting variability in the bootstraps (Figure S5).

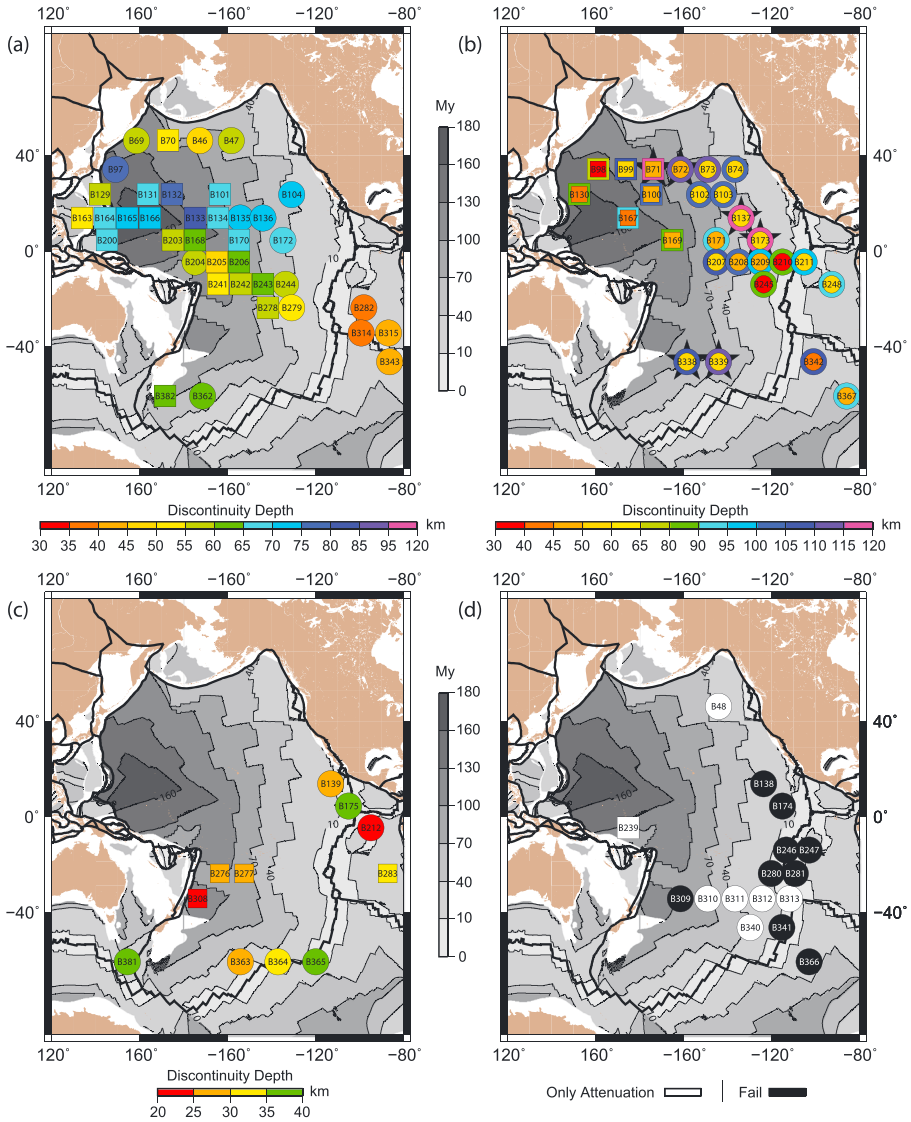

Figure 3. Pacific 10° *SS* bounce point bins with discontinuity depths. Numbers within the symbols indicate Pacific bin numbers. The colored circles and squares correspond to discontinuity depths for normal and anomalous lithosphere, respectively, for (a) single discontinuity, (b) double discontinuity, and (c) positive discontinuity. The overlapping circles and squares in Figure 3b correspond to double discontinuity with the outer color showing depth of deeper discontinuity and inner circle showing depth of shallow discontinuity. Six bins encircled by black stars indicate explicit double discontinuity. (d) The white bins require only attenuation to fit the data. The black bins could not be resolved. Depth scales are different for maps (Figures 3a–3c). The background colors show seafloor age with age contours (thin black lines) at an interval of 30 Myr [*Müller et al.*, 2013]. The thick black lines represent plate boundaries [*Bird*, 2003].

We test for the significance of model parameters beyond the attenuated reference stack by using an *F* test for significance of regression [*Draper and Smith*, 1998; *Hosmer et al.*, 1997]. The number of degrees of freedom in the data waveforms was determined by using autocorrelation of an *SS* waveform generated by using all of the waveforms in the 10° Pacific bins. We estimated 11 degrees of freedom in the data in the time window used in the inversions. Our final result resolves four model parameters for the single discontinuity (attenuation + one discontinuity), seven model parameters for the double discontinuity (attenuation + two discontinuities), and four model parameters for the positive discontinuity (attenuation + one discontinuity). Since we include a constant oceanic crust of 7 km (section 2.4), the Moho corresponds to one fixed parameter. Each discontinuity corresponds to three free model parameters (depth, amplitude, and Gaussian width), and attenuation corresponds to one free model parameter (t^*). The effect of varying parameters (depth,

Table 1. Bins Marked "N" Represent Predominantly Normal Oceanic Crust and Those Marked "A" Represent Predominantly Anomalous Oceanic Crust [*Korenaga and Korenaga*, 2008][a]

Bin	Type	Lon	Lat	Bounces	Age ($Myr^{1/2}$)	Depth (km)	Depth Bounds (km)	Amplitude (%)	Sharpness (km)	Attenuation (s)	Interpretation
139	N	−113	15	421	4	28	25–32	14	2	6.4	Moho
175	N	−105	5	370	3	36	35–39	15	2	6.4	Moho
212	N	−95	−5	483	3	20	19–24	5	2	6.4	Attenuation
276	A	−163.6	−25	304	10	29	25–33	7	2	6.4	Moho
277	A	−152.7	−25	380	9	27	24–30	10	2	6.4	Moho
283	A	−87.3	−25	345	5	31	28–34	2	2	6.4	Moho
308	A	−173.8	−35	292	10	20	19–24	3	2	6.4	Moho
381	N	154.3	−55	369	5	37	35–39	5	2	6.4	Moho
363	N	−154.3	−55	523	5	26	23–30	3	2	6.4	Attenuation
364	N	−137	−55	506	5	33	29–35	3	2	6.4	Attenuation
365	N	−120	−55	361	5	36	32–38	5	0	5.3	Moho

[a]Depth scaling is described in section 2.5. We do not include a 7 km oceanic crust for modeling these bins. Amplitude refers to the shear velocity drop (percent) in depth. Sharpness refers to width of the Gaussian operator, represented by $\pm 1\sigma$, i.e., 2 times the Gaussian half-width.

amplitude, and sharpness) on the models is illustrated in Figure S4, and the trade-off between these model parameters is illustrated in Figure S5.

The best fitting model parameters were used to determine the depth, sharpness, and amplitude of the velocity discontinuities. Operator amplitudes were scaled to velocity variation by using the equation for *SS* reflection coefficient [*Aki and Richards*, 2009], assuming a constant mantle density of $3.38\,g\,cm^{-3}$ and an incidence angle of 26.7°. Although we use a constant density, we note that *SS* is affected by both density and velocity, and we do not have the ability to distinguish between the two. Similarly, depth was scaled from the delay time of the operator, which is a function of the two-way travel time between the discontinuity and the free surface [*Aki and Richards*, 2009]. The depth scaling was done assuming a constant oceanic crustal thickness of 7 km, crustal velocity of 3.75 km/s, an upper mantle velocity of 4.55 km/s, and an average horizontal slowness of 0.12 s/km. We assumed a plane wave approximation for our calculations. Discontinuity depths were also estimated by using the velocity model of *Nishimura and Forsyth* [1989], but there was no significant change (±5 km) in the discontinuity depths compared to our depth estimates using a fixed crustal and mantle velocities. Discontinuity sharpness was governed by the width of the Gaussian operator and is reported as ±1 standard deviation or twice the Gaussian half-width. Although the velocity change may occur over a total depth range of 4 times the Gaussian half-width.

Variation in the arrival time of the precursor phase from moveout for the range of event-to-station distances used here is minimal, having little effect on our result. The moveout on our deepest interpreted phase (120 km) for our 90–180° epicentral distance range is <3 s (Figure S6). Furthermore, 95% of the waveforms in our stacks arrive from an epicentral distance of 90°–150° (Figure S1), which only gives an ~1.6 s difference in arrival time from moveout. This is much less than one fourth of the dominant wave period (20 s) used in our study. Therefore, while moveout may slightly affect our constraints on the sharpness of the discontinuities making them appear slightly more gradual, it does not significantly affect our ability to image the discontinuities <120 km in depth. In practice, the effect of moveout is incorporated within the error limits from the bootstrap.

3. Results

We resolve lithospheric discontinuity structure in 82 out of 91 bins in the Pacific with significantly increased lateral coverage across the Pacific than in previous studies (Figure 3) [*Rychert and Shearer*, 2011; *Schmerr*, 2012]. We image a pervasive negative discontinuity, i.e., velocity decrease with depth, at 30–80 km depth in 64 bins. We also image some complexities: locations with a shallow positive discontinuity (20–36 km), locations with no discontinuities, and locations where the negative gradient continues to greater depth.

3.1. Shallow, Positive Discontinuity

We resolve a positive discontinuity in 11 out of 91 bins in the Pacific, 8 of which sample relatively young <30 Myr lithosphere and 3 bins sample >90 Myr lithosphere (Figure 3c and Table 1). The results here do not include an oceanic Moho at 7 km depth. Once we established these 11 bins required a shallow

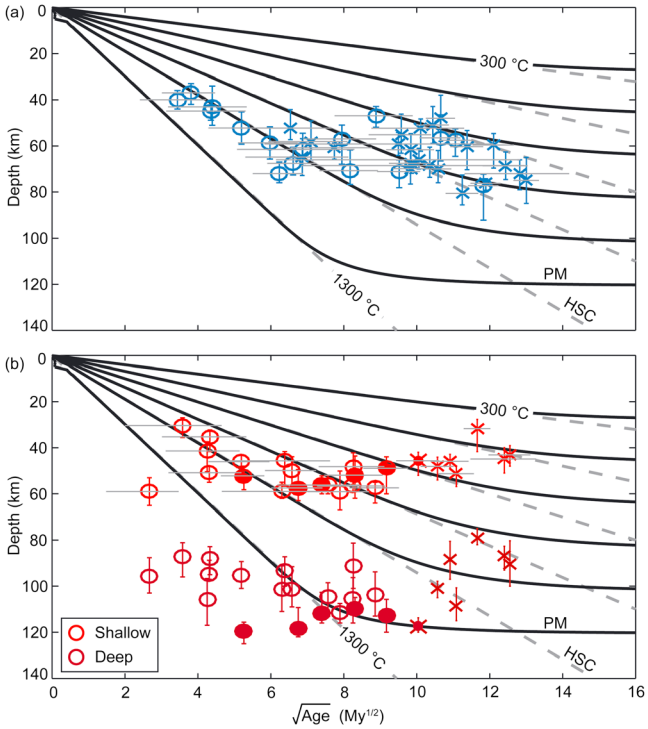

Figure 4. Discontinuity depth versus square root of seafloor age for (a) single discontinuity and (b) double discontinuity. The circles and crosses represent normal and anomalous lithosphere, respectively. The darker circles and crosses in Figure 4b show depths of deeper discontinuity. The symbols with filled colors indicate bins with explicit double discontinuity. The solid black lines show plate model (PM) [*Stein and Stein*, 1992], assuming a potential temperature of 1350°C and a plate velocity of 60 mm/yr, isotherms from 300°C to 1300°C at an interval of 200°C. The dashed grey lines show half-space cooling (HSC) model isotherms from 300°C to 1300°C. The horizontal error bars in Figures 4a and 4b represent the age of seafloor to one standard deviation in each bounce point bin. The vertical error bars indicate 95% confidence bounds on depth range.

positive discontinuity, we took out the Moho at 7 km depth that was assumed for the rest of the bins, since these shallow positive discontinuities may represent thickened crust. However, including an oceanic Moho at 7 km depth had no significant effect on our results. The discontinuity is quite sharp at depths ranging from 20 to 36 km and velocity contrast of 2 to 15% (average velocity contrast of 8%). We do not resolve any positive discontinuities at depths greater than 36 km. Waveform fits for the positive discontinuity are shown in Figure S7.

3.2. Pervasive, Negative Discontinuity

We resolve a single sharp negative discontinuity in 64 bins, 38 of which require a single negative discontinuity (Figures 3a and 4a and Table 2) and 26 of which require a shallow and a deeper negative discontinuity (Figures 3b and 4b and Table 3). Here we discuss the shallow pervasive discontinuity, i.e., the best fit depth from 38 single-discontinuity bins and the shallow discontinuity depth from the 26 double-discontinuity bins as a single result. The depth of the shallow discontinuity varies from 30 to 72 km according to the conductive cooling model until 36 Myr along a 1100°C thermal contour. We use a piecewise linear fit to the age-depth data to estimate the breakpoint where there is a change in slope in the data. The inversion yields a breakpoint of 36 ± 9 Myr with a slope of 8.9 ± 4.7 km/Myr$^{1/2}$ from 0 to 36 Myr and −0.4 ± 2.7 km/Myr$^{1/2}$ from 36 to 180 Myr. The error bars indicate 2 sigma variation. There is no age dependence after ~36 Myr, and the discontinuity appears to flatten in the depth range of 43–80 km, an average depth of 60 km (Figure 4), and a 1.5 km standard error of the mean. Waveform fits to the data for bins with a single negative discontinuity are shown in Figure S8 and for bins with double discontinuity are shown in Figure S9. The shallow discontinuity is generally sharp with velocity contrast of 3–15%, an average velocity contrast of 7 ± 2% occurring over < 21 km (Tables 2 and 3). Some bins require a wide Gaussian operator that suggests that the velocity contrast occurs over a greater depth range and/or the lithospheric thickness varies laterally in the sampled region. Although we use a piecewise liner fit to determine the breakpoint age in our data, 36 ± 9 Myr, there is strong correlation between depth and square root of seafloor age <50 Myr, at 0.68 (including bin 211) and 0.82 (excluding bin 211).

3.3. Resolution of the Shape of the Velocity Gradient

In the 26 bins described above, a deeper negative discontinuity at 80–120 km depth is required along with a shallow negative discontinuity to fit the data. We could not resolve any bin that requires a shallow positive and a deeper negative or vice versa. Further, we tested to see if two negative discontinuities could be replaced by a single discontinuity with a large Gaussian width. Only bin 98 could be resolved with a simple single wide Gaussian operator but has a statistical better fit with the data using a double negative

Table 2. Bins Marked "N" Represent Predominantly Normal Oceanic Crust and Those Marked "A" Represent Predominantly Anomalous Oceanic Crust [*Korenaga and Korenaga*, 2008][a]

Bin	Type	Lon	Lat	Bounces	Age ($Myr^{1/2}$)	Depth (km)	Depth Bounds (km)	Amplitude (±2%)	Sharpness (±4 km)	Attenuation (s)
46	N	−172.8	45	2883	9	47	43–52	6	19	4.0
47	N	−158.4	45	1839	8	57	51–68	14	16	4.1
69	N	158.4	45	1943	11	58	53–65	6	10	3.4
70	A	172.8	45	3055	10	52	48–62	5	20	4.0
97	N	148.9	35	1256	12	77	72–92	7	10	3.8
101	A	−163.6	25	4532	10	70	69–72	12	10	6.0
104	N	−130.9	25	644	6	72	67–76	9	9	5.0
129	A	141.8	25	1102	9	59	54–64	10	22	3.0
131	A	163.6	25	1023	12	69	63–75	4	15	3.0
132	A	174.5	25	1795	12	76	74–79	13	10	4.5
133	A	−174.8	15	1755	11	81	73–86	14	10	4.4
134	A	−164.6	15	3203	11	70	62–76	15	8	6.0
135	N	−154.3	15	3540	10	71	66–78	9	11	6.0
136	N	−144	15	2748	8	71	62–77	3	13	6.0
163	A	133.7	15	969	7	52	44–57	11	16	3.3
164	A	144	15	816	10	66	61–70	4	18	3.7
165	A	154.3	15	987	13	72	66–79	3	17	3.0
166	A	164.6	15	1018	13	75	65–85	5	9	3.0
168	A	−175	5	392	11	60	53–70	3	10	3.0
170	A	−155	5	1093	10	68	62–77	3	11	5.9
172	N	−135	5	1016	7	68	61–73	5	9	5.8
200	A	145	5	586	10	69	61–74	14	21	4.5
203	A	175	5	459	12	60	55–70	9	14	3.9
204	N	−175	−5	290	11	57	47–67	12	12	3.2
205	A	−165	−5	571	11	48	38–58	6	9	3.0
206	A	−155	−5	1091	10	62	55–70	6	13	4.4
241	A	−164.5	−15	532	10	51	43–59	9	9	4.5
242	A	−154.3	−15	853	10	55	46–63	9	16	4.4
243	A	−144	−15	893	8	61	59–66	4	17	5.6
244	N	−133.7	−15	835	6	59	52–66	15	10	4.5
278	A	−141.8	−25	526	7	58	49–66	12	15	6.0
279	N	−130.9	−25	491	5	52	45–59	7	9	3.0
282	N	−98.2	−25	295	4	37	33–42	4	5	3.0
314	N	−99.3	−35	284	3	40	36–44	9	6	5.2
315	N	−86.9	−35	302	4	45	41–49	13	9	3.3
343	N	−86.4	−45	289	4	43	34–51	13	9	3.3
362	N	−171.4	−55	486	7	61	54–68	12	20	6.0
382	A	171.4	−55	356	7	65	57–73	6	19	6.0

[a]Depth scaling is described in section 2.5. These bins include a 7 km thick oceanic crust as described in section 2.4. Amplitude refers to the shear velocity drop (percent) in depth. Sharpness refers to width of the Gaussian operator, represented by $\pm 1\sigma$, i.e., 2 times the Gaussian half-width.

discontinuity. One reason a single wide Gaussian operator cannot easily replace two discontinuities is that interference at shallow depth with the main *SS* pulse causes a bad fit. This can be avoided with irregularly shaped pulses, which we also tested.

We could fit 20 bins with a single skewed Gaussian operator out of 26 bins that have double discontinuity. Only six (bins 71, 72, 137, 173, 338, and 339) could not be resolved and require a double discontinuity (Figure 4). These six bins also have the appearance of a double pulse (Figure S9). The skewed functions for the double discontinuity bins are best fit with a sharp Gaussian at shallow depths, followed by a rectangular function and a gradual Gaussian tail at the end (Figure 5). In most cases the models converge to a solution where there is a sharp discontinuity at shallow depths followed a more gradual tail (large Gaussian width).

The skewed operator test suggests that while we can resolve the existence of velocity discontinuities, there is some uncertainty in the exact shape. We cannot distinguish between two sharp discontinuities with a linear gradient (skewed Gaussian) between them (Figure S10). We report the depths of the asymmetric operators as both the maximum amplitude (hereafter referred to as SG depths) and as the depth of half the total velocity drop (hereafter referred to as CDF depths). In case of bins with a single discontinuity (Table 2), we did not find

Table 3. Bins Marked "N" Represent Predominantly Normal Oceanic Crust and Those Marked "A" Represent Predominantly Anomalous Oceanic Crust [*Korenaga and Korenaga*, 2008][a]

Bin	Type	Lon	Lat	Bounces	Age ($Myr^{1/2}$)	Depth 1 (km)	Depth Bounds (km)	Amplitude 1 (±2%)	Sharpness 1 (±3 km)	Depth 2 (km)	Depth Bounds (km)	Amplitude 2 (±1%)	Sharpness 2 (±3 km)	Attenuation (s)
71*	A	−173.8	35	2936	10	46	42–52	4*	5*	118	114–120	5*	7*	5.7*
72*	N	−161.4	35	2731	9	49	44–60	5*	7*	113	106–120	3*	2*	4.3*
73	N	−149	35	1367	8	59	50–67	4	0	112	108–116	5	8	6.0
74	N	−136.6	35	448	6	59	55–62	10	6	101	91–111	3	2	4.9
98	A	161.4	35	1241	12	32	28–42	6	10	79	75–82	3	5	5.1
99	A	173.8	35	2857	11	51	48–57	5	9	109	101–115	4	3	3.7
100	A	−174.5	25	2856	11	48	44–54	5	8	101	98–105	7	10	3.7
102	N	−152.7	25	2667	9	57	55–64	5	10	104	94–113	2	2	5.2
103	N	−141.8	25	1381	8	56	52–60	5	8	105	99–113	2	2	5.3
130	A	152.7	25	678	12	45	40–51	9	6	87	83–93	3	2	4.5
137*	N	−133.7	15	1455	7	57	49–63	4*	6*	118	109–122	3*	2*	5.3*
167	A	174.9	15	695	13	43	39–48	4	2	90	80–100	6	5	5.0
169	A	−165	5	642	11	46	43–49	7	9	89	81–97	3	2	3.9
171	N	−145	5	2116	8	48	42–55	11	15	91	81–101	2	2	6.0
173*	N	−125	5	830	5	52	48–58	4*	6*	120	116–125	4*	5*	3.0*
207	N	−145	−5	1235	8	57	55–59	6	4	105	96–116	4	5	3.0
208	N	−135	−5	1619	7	50	44–59	4	5	102	92–109	8	10	5.4
209	N	−125	−5	927	5	46	43–48	7	8	95	89–101	3	2	3.7
210	N	−115	−5	647	4	30	27–35	5	5	87	81–96	7	11	3.0
211	N	−105	−5	689	3	59	53–65	4	6	96	88–103	5	3	3.0
245	N	−123.4	−15	514	4	35	32–41	4	5	88	83–95	6	5	3.0
248	N	−92.6	−15	649	4	51	48–55	4	11	95	89–97	3	2	5.5
338*	N	−158.4	−45	580	8	52	44–62	9*	10*	110	105–113	2*	2*	4.4*
339*	N	−144	−45	749	7	56	52–60	11*	8*	112	103–116	3*	2*	6*
342	N	−100.8	−45	324	4	41	37–50	13	10	106	97–117	3	40	4.1
367	N	−85.7	−55	295	6	46	42–57	6	8	93	87–100	2	2	4.8

[a]Depth scaling is described in section 2.5. These bins include a 7 km thick oceanic crust as described in section 2.4. Depth 1, Amplitude 1, and Sharpness 1 refer to the shallow discontinuity, and Depth 2, Amplitude 2, and Sharpness 2 refer to the deeper discontinuity. Both shallow and deeper discontinuities are of negative sign, i.e., velocity decrease with depth. Amplitude refers to the shear velocity drop (percent) in depth. Sharpness refers to width of the Gaussian operator, represented by $\pm 1\sigma$, i.e., 2 times the Gaussian half-width.

any significant change in discontinuity depths when skewed Gaussian operators were used (Figure S11). The CDF depths are $< \pm 3$ km, and the SG depths are $< \pm 6$ km compared to discontinuity depths calculated by using symmetric Gaussian functions. In case of bins with a double discontinuity the fits to the data using skewed Gaussian operators are statistically similar or better in some cases compared to the fits to the data using two Gaussian operators (Figure S12). The SG depths are $< \pm 5$ km compared to the previously reported shallow discontinuity from the double-discontinuity bins and shows similar age-depth trend (Figure 5a). But the CDF depths are much deeper, generally occurring midway between the shallow and deeper discontinuity (Figure 5b). The CDF depths are in the range of 55–90 km, average depth of ~75 km, and show no apparent age dependency. The SG depths are probably the most important since *SS* is most sensitive to the depth of the strongest and sharpest velocity change.

3.4. No Discontinuity and Failed Bins

Nine bins could not be resolved at all owing to small number of waveforms and/or noise (Table 4). Seven bins could be modeled with attenuation alone, allowing a maximum of 6.4 s, and required no additional discontinuity (Figure 3d and Table 4). Waveform fits to the data are shown in Figure S13.

4. Discussion

4.1. Shallow, Positive Discontinuity

Resolution of the shallowest discontinuities ($<$30 km) is difficult since phases arrive very close to the main *SS* phase and can trade-off with the attenuation operator. We investigate this trade-off for the shallow positive discontinuities. We typically allow attenuation operators of 3–6 s in our inversions (section 2.4), but all bins with a positive discontinuity are better fit with a larger attenuation operator (Table 1). If we allow a maximum

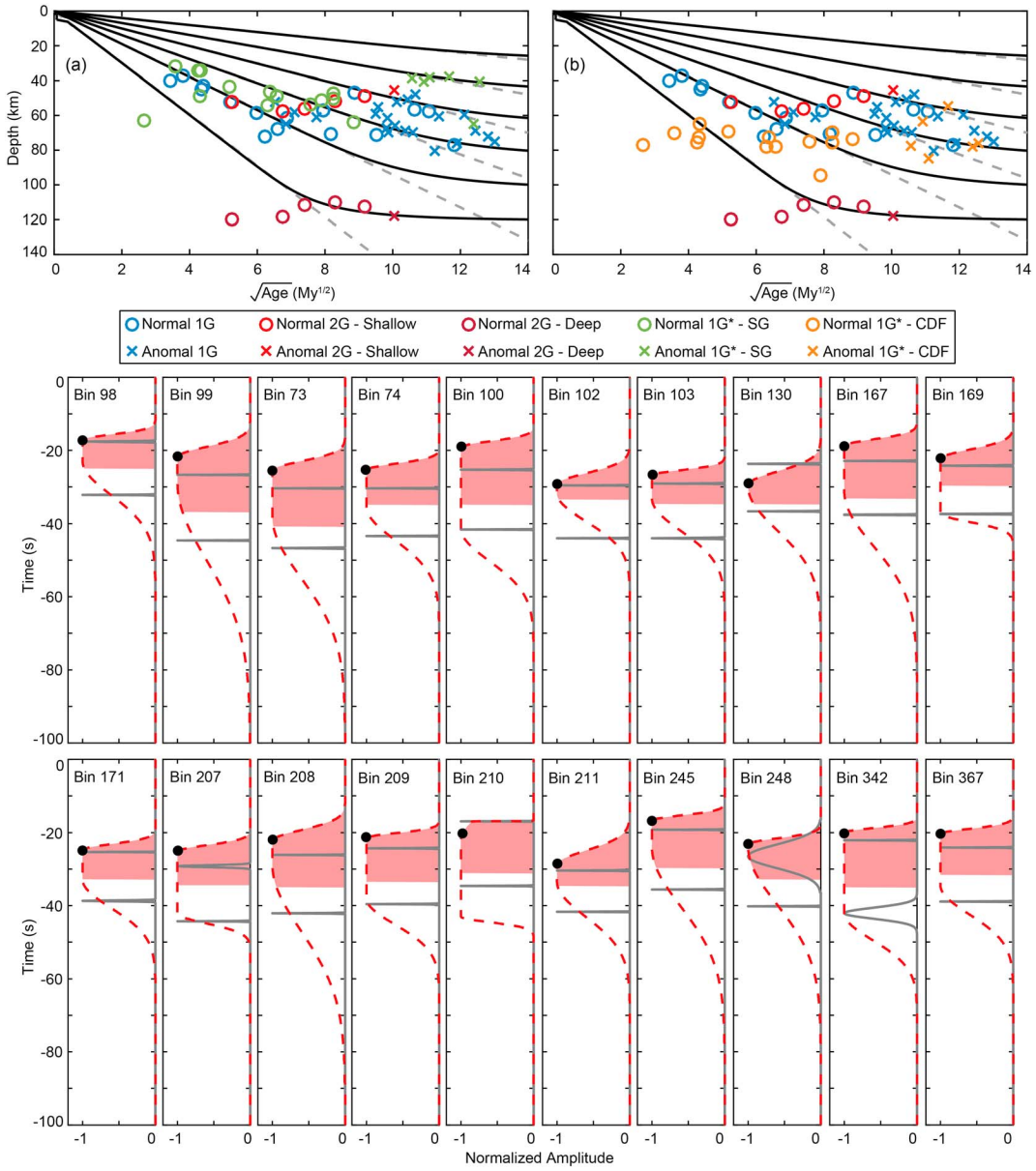

Figure 5. (a and b) Discontinuity depth results for bins with double discontinuity modeled by using a skewed Gaussian operator. The SG depths are plotted in Figure 5a and the CDF depths in Figure 5b. The bottom plots show bins that could be equally well fit by a skewed Gaussian operator (dashed red) or a double discontinuity (two Gaussian) operator (solid grey). The black circle shows the delay time at which the SG depths are calculated. The red shaded area is used to calculate the CDF depths. "Normal" and "Anomal" refers to normal and anomalous bins (Table 3). "G" represents a Gaussian, and "G*" represents a skewed Gaussian operator. Numbers "1" and "2" represent the number of operators used.

attenuation of 6.4 s, only 8 of 11 bins require a positive discontinuity, although the depth and sharpness constraints in these bins remain unchanged.

Several of our bins with a shallow, positive discontinuity are located in regions that have been altered by volcanism and may represent a thickened crust (marked as "Moho" in Table 1). For example, bins 276 and 277 sample the Manihiki Plateau and bin 308 samples the Hikurangi plateau. Manihiki and Hikurangi plateaus are thought to have been part of a much larger Ontong Java super plateau that formed due to a massive volcanic event 120 Myr ago [*Taylor*, 2006]. The ~25 km thick crust that we image is consistent with previous crustal thickness estimates of 15–25 km from seismic reflection survey and gravity modeling [*Davy et al.*, 2008; *Davy and Wood*, 1994]. Bin 175 samples the Galapagos archipelago, and the thicker crust,

Table 4. Bins Marked "N" Represent Predominantly Normal Oceanic Crust and Those Marked "A" Represent Predominantly Anomalous Oceanic Crust [*Korenaga and Korenaga*, 2008][a]

Bin	Type	Lon	Lat	Bounces	Age (Myr$^{1/2}$)	Depth (km)	Attenuation (s)
48	N	−144	45	689	6		3.1
239	A	175	−5	269	11		3.4
310	N	−149	−35	469	9		6.4
311	N	−136.6	−35	444	7		4.6
312	N	−124.1	−35	454	5		3.0
313	N	−111.7	−35	357	3		5.5
340	N	−129.6	−45	468	6		4.4
138	N	−123.4	15	573	5	Fail	
174	N	−115	5	186	4	Fail	
246	N	−113.1	−15	263	3	Fail	
247	N	−102.6	−15	175	3	Fail	
280	N	−120	−25	265	3	Fail	
281	N	−109.1	−25	87	2	Fail	
309	N	−161.4	−35	150	10	Fail	
341	N	−115.2	−45	280	3	Fail	
366	N	−102.8	−55	119	6	Fail	

[a]Bins that have no depth value require no additional discontinuity and can be fit with attenuation alone. Bins marked "Fail" are noisy and have insufficient waveforms.

~35–40 km, that we image is consistent with receiver function study in the region that has reported a velocity increase at 37 ± 7 km depth [*Rychert et al*., 2014a]. Bin 283 is near the eastern hot spot track/Nazca Ridge and may reflect thickened crust. The positive discontinuity in bin 139 can be explained by its proximity to the southern margin of the North American continent which has a crustal thickness of 20–35 km [*Laske et al*., 2012], sampled by the large Fresnel zone (~10°) of the *SS* (Figure S2). Finally, bins 365 and 381 are both located on mid-ocean ridges but require a positive discontinuity at 36 and 37 km depth even if very high attenuation (6.8 s) is assumed. If very large attenuation of >6.8 s is allowed, 5 (bins 212, 283, 308, 363, and 364) out of 11 bins require no additional discontinuity (Figure 6), four (bins 212, 363 363, and 364) that are located near mid-ocean ridges and might be characterized by higher than average attenuation [*Dalton et al*., 2008].

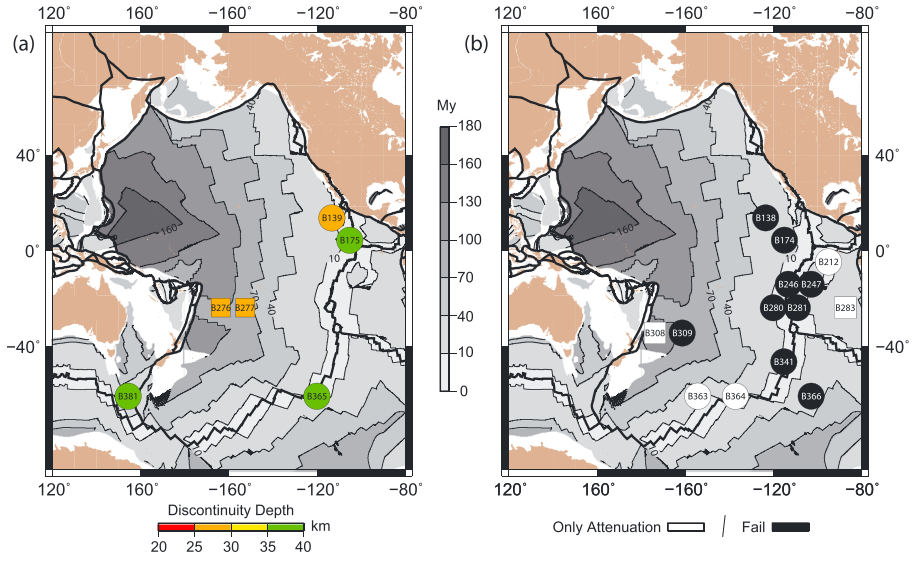

Figure 6. (a and b) Pacific 10° *SS* bounce point bins with discontinuity depths allowing for higher attenuation. Numbers within the symbols correspond to Pacific bin numbers. The circles and squares show normal and anomalous lithosphere, respectively. The colors in Figure 6a show depth of positive discontinuity. The white bins in Figure 6b require only attenuation to fit the data. The black bins could not be resolved. The background colors show seafloor age with age contours (thin black lines) at an interval of 30 Myr [*Müller et al*., 2013]. The thick black lines represent plate boundaries [*Bird*, 2003].

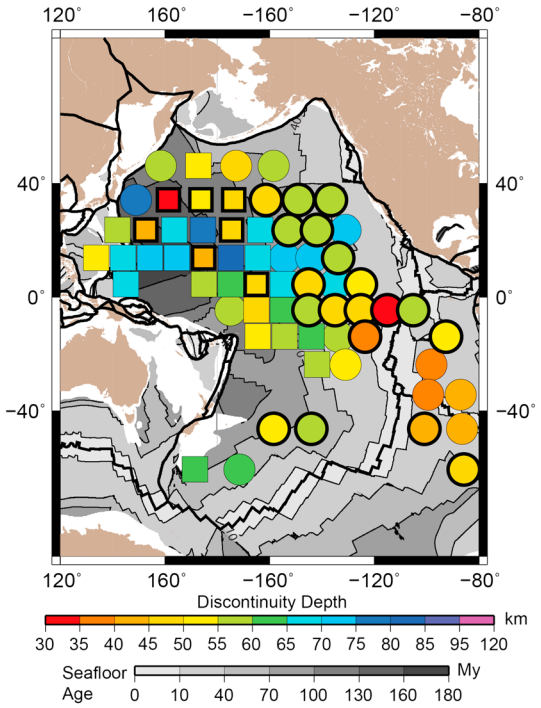

Figure 7. The shallow discontinuity at ~60 km is pervasive across most of the Pacific. The circles and squares show normal and anomalous bins, respectively. Bins with no black outline show single negative discontinuity (Figure 3a). Bins with a thick black outline show shallow discontinuity from the double discontinuity bins (Figure 3b). The background colors show seafloor age with age contours (thin black lines) at an interval of 30 Myr [*Müller et al.*, 2013]. The thick black lines represent plate boundaries [*Bird*, 2003].

4.2. Pervasive, Negative Discontinuity

4.2.1. Comparison to Previous Studies

Our results for the shallow, pervasive negative discontinuity (Figure 7) in the depth range of 30–80 km are in agreement with a previous study using *SS* precursors that imaged a sharp (4–13% over <70 km) age-dependent discontinuity at 25–70 km depth beneath young seafloor (<40–70 Myr) [*Rychert and Shearer*, 2011]. Our depths are only slightly deeper than RS11. Our results show greater depth-age dependence beneath young seafloor than those of *Schmerr* [2012] (Figure 8).

Our results for younger oceans are also supported by receiver function studies of oceanic stations in the northwest Pacific that image a sharp (7–8% velocity reduction over 10–15 km) discontinuity at 55 km and 76 km with a plate age of 25 Myr and 49 Myr in the Philippine sea [*Kawakatsu et al.*, 2009] (Figure 8). Further, a discontinuity in the depth range of 51–92 km that progressively increases with age from 9 to 70 Myr was also imaged by using receiver functions along three oceanic plate margins in the Pacific [*Kumar and Kawakatsu*, 2011].

Our discontinuity depth results beneath young seafloor, <36 Myr (as determined by piecewise linear fit to the age-depth data), are also in general agreement with surface wave results that image a thickening lithosphere with age in both global [*French et al.*, 2013; *Maggi et al.*, 2006; *Nettles and Dziewonski*, 2008; *Nishimura and Forsyth*, 1989] and regional studies [*Gu et al.*, 2005; *Harmon et al.*, 2009]. For example, our discontinuity depth results are in good agreement with the depth of the negative gradient in Voigt average isotropic shear velocity in a global surface wave model, SEMum2 [*French et al.*, 2013] (Figure 9). We image a discontinuity in the depth range of 30–59 km compared to a discontinuity at 38–56 km in SEMum2 beneath similarly young seafloor (Figure 9b). However, the discontinuity we image is sharper, an average velocity contrast of ~7–8% occurring over <21 km compared to an average velocity drop of ~3.5% occurring over ~65 km in global surface wave models [*French et al.*, 2013].

The discontinuity depths we image in the older (>36 Myr) lithosphere appears to be at a near constant depth of ~60 km, cutting across isotherms from half-space cooling and plate models. The near constant depth discontinuities that we image are similar to those imaged in the depth range of 40–80 km [*Gaherty et al.*, 1999; *Tan and Helmberger*, 2007], 40–100 km [*Schmerr*, 2012], and 60–94 km beneath old seafloor [*Kumar and Kawakatsu*, 2011] (Figure 8). Our results are also broadly consistent with the mean depth of the gradual drop in velocity with depth in surface wave models in most locations, although surface waves tend to be systematically deeper, by ~10 km (mean depth ~75 km) with two locations much deeper (~130 km) [*French et al.*, 2013] (Figure 9).

Our results beneath older seafloor are also in agreement with the 6–12% velocity drop at 40–100 km depth beneath seafloor >36 Myr [*Rychert and Shearer*, 2011] (Figure 8) but suggest a much more pervasive feature than previously detected (Figure 7). Our results are shallower (50–80 km) than the four deep (95–130 km

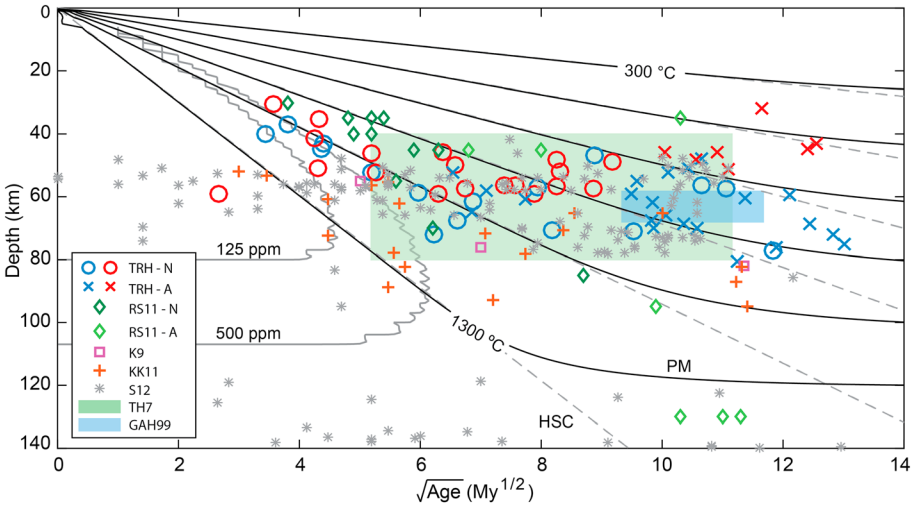

Figure 8. Depth of the shallow, pervasive discontinuity compared to seafloor age and plate model (PM)/half-space cooling (HSC) isotherms. The present study is referred to as TRH. The circles and crosses correspond to normal (TRH-N) and anomalous lithosphere (TRH-A), respectively. The blue "circle"/"cross" shows results of single discontinuity, and the red circle/cross shows results of shallow discontinuity in bins with double negative discontinuity. The diamonds show *SS* precursor results for normal (RS11-N) and anomalous (RS11-A) lithosphere from RS11 [*Rychert and Shearer*, 2011]. The squares and plus signs show LAB depths from receiver function studies of K9 [*Kawakatsu et al.*, 2009] and KK11[*Kumar and Kawakatsu*, 2011]. The stars (S12) show discontinuity from previous *SS* precursor study [*Schmerr*, 2012]. The colored boxes show results from TH7 [*Tan and Helmberger*, 2007] and GAH99 [*Gaherty et al.*, 1999]. The solid grey lines show melt contours for a mantle melting model with varying amounts of water (ppm) [*Katz et al.*, 2003]. The solid black lines show isotherms for plate model [*Stein and Stein*, 1992], and the dashed grey lines show isotherms for half space cooling model.

depth) bins from RS11 (bins 70, 71, 99, and 132). This is likely related to uncertainty in gradient shape and also an artifact of the different parameterizations of the two studies. RS11 only allowed a single negative discontinuity, and thus required broad gradients in these bins. The gradients were tapered on the source side to avoid interference, and the peak of the Gaussian was reported. This would be more similar to our skewed results for double discontinuity bins. This could reconcile depth differences between bins 71 and 99, which were also fit by a wide skewed or a double discontinuity operator here and also bin 99 which had a large Gaussian width in RS11, leaving only bin 132 discrepant. Overall, the resolution and parameterization here are improved from the past since our larger data set, with better quality control, allows for better constraints on the character of the gradient.

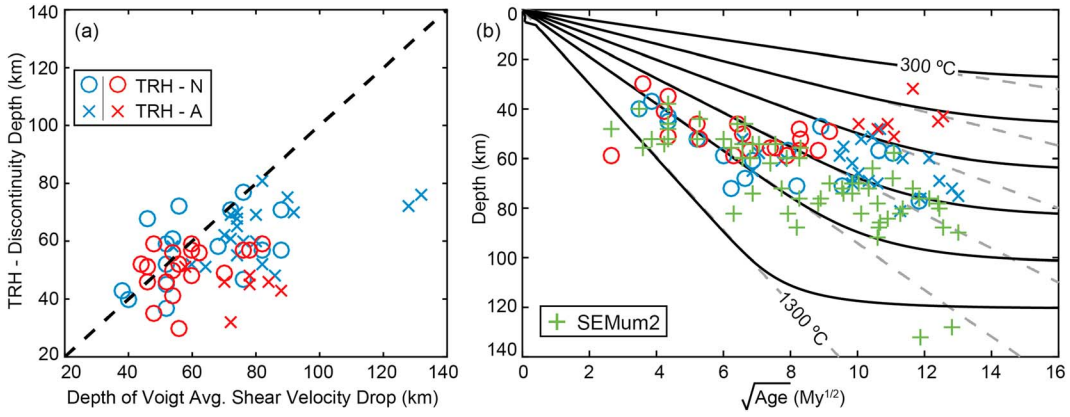

Figure 9. (a) Shallow discontinuity depths compared to depth of the negative gradient in Voigt average shear velocity in a global surface wave model, SEMum2 [*French et al.*, 2013]. TRH refers to the present study. The circles and crosses correspond to normal (TRH-N) and anomalous lithosphere (TRH-A). (b) Discontinuity depths from present study and depths estimated from SEMum2 plotted against square root of seafloor age.

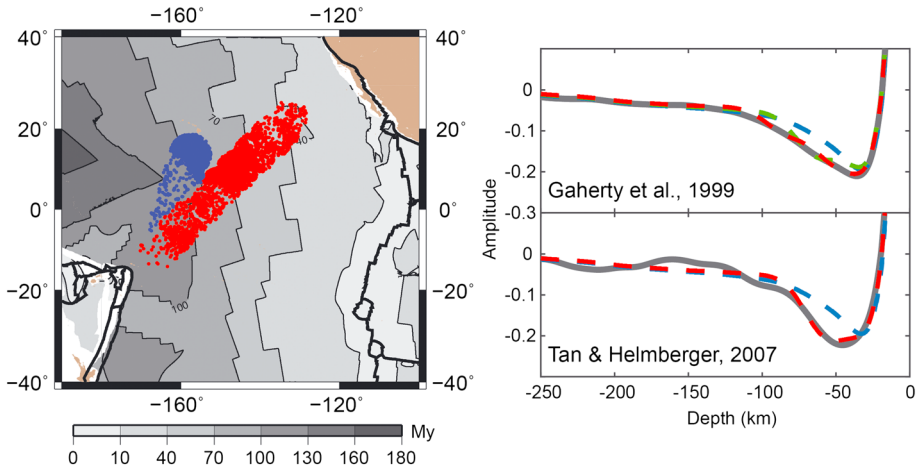

Figure 10. Bounce points included in the stacks that approximate the Pacific transects, PA5 (blue) [*Gaherty et al.*, 1999] and PAC06 (red) [*Tan and Helmberger*, 2007]. The background colors show seafloor age [*Müller et al.*, 2013]. Waveform fits for the two transects are shown on the right. The solid grey line is the data, the dashed blue is the attenuated reference *S* wave, the dashed red is the best fit model, and the dashed green in the top plot is best fit model using a single discontinuity.

4.2.2. Comparison to Previous Transect Studies

We also compare our results to the pacific transects PA5 [*Gaherty et al.*, 1999] and PAC06 [*Tan and Helmberger*, 2007] (Figure 10). For this comparison we generated data and reference stacks, using the procedure described in section 2, to approximate the pacific transects PA5 and PAC06. The depth scaling was done assuming a constant oceanic crustal thickness of 7 km, crustal velocity of 3.75 km/s, an upper mantle velocity of 4.55 km/s, and an average horizontal slowness of 0.12 s/km. We resolve a sharp discontinuity, ~6% velocity contrast over $<$10 km at a depth of 40–60 km compared to the ~6% velocity change in the depth range of 40–80 km reported by PAC06 study [*Tan and Helmberger*, 2007]. Similarly, we resolve an ~6% velocity contrast over $<$15 km at a depth range of 42–73 km along the PA5 transect compared to a sharp ($<$30 km thick) 6% velocity drop at a relatively constant depth of 60 ± 20 km [*Gaherty et al.*, 1999]. The discontinuity along PAC06 appears to be sharper than along PA5 transect. But the PA5 transect fits better with a sharper double negative discontinuity at 45 km and 70 km with a velocity contrast of 5–6% occurring over $<$10 km. The fact that our *SS* precursors also require sharp discontinuities in the similar depth range along PA5 and PAC06 transects suggests that mechanisms other than temperature alone are required.

The discontinuity that we image along PA5 and PAC06 agree with the best fit result from RS11, a 3–10% change over $<$50 km [*Rychert and Shearer*, 2011]. However, a discontinuity was not statistically required along PA5 and PA06 in RS11. The improvement in resolution here is probably from our larger data set, additional quality checks that we impose and also a different back azimuth distribution, primarily 50°–90°, in comparison to the W-E back azimuths that dominated RS11. Our stacks excluding the 50°–90° back azimuth range show a reduction in amplitude for the two transects, suggesting an azimuthal anisotropic component to the discontinuity [*Rychert et al.*, 2014b; *Rychert et al.*, 2012]. When we limit the back azimuth range considered here to that of RS11, we can no longer resolve a significant discontinuity along PA5. However, PAC06 could be resolved to within ±4 km.

4.2.3. Comparison to a Thermal Model

Our results show that the shallow, negative discontinuity beneath young ocean, $<$36 Myr as determined by piecewise linear fit, increases in depth from 30 to 80 km with increasing seafloor age. This result is consistent with a thermally defined lithosphere that thickens with age (Figure 8), falling along the 1100°C isotherm. To test a thermal origin for the Pacific lithospheric discontinuities, we considered experimental predictions for seismic velocity [*Jackson and Faul*, 2010] (hereafter referred to as JF10) from a half-space cooling (HSC) and plate model (PM) [*Stein and Stein*, 1992]. We assume a grain size of 20 mm [*Behn et al.*, 2009] and mantle potential temperature of 1350°C. The anelastic effects (velocities deeper than the kink in the profiles) are frequency-dependent. Here we assume surface wave frequency-depth relationships [*Forsyth*, 1992], although the frequency effect is not strong [*Rychert et al.*, 2008]. The predicted seismic velocity gradients are sharper for younger ages and more gradual beneath old seafloor (Figure 11). We estimate the discontinuity depth

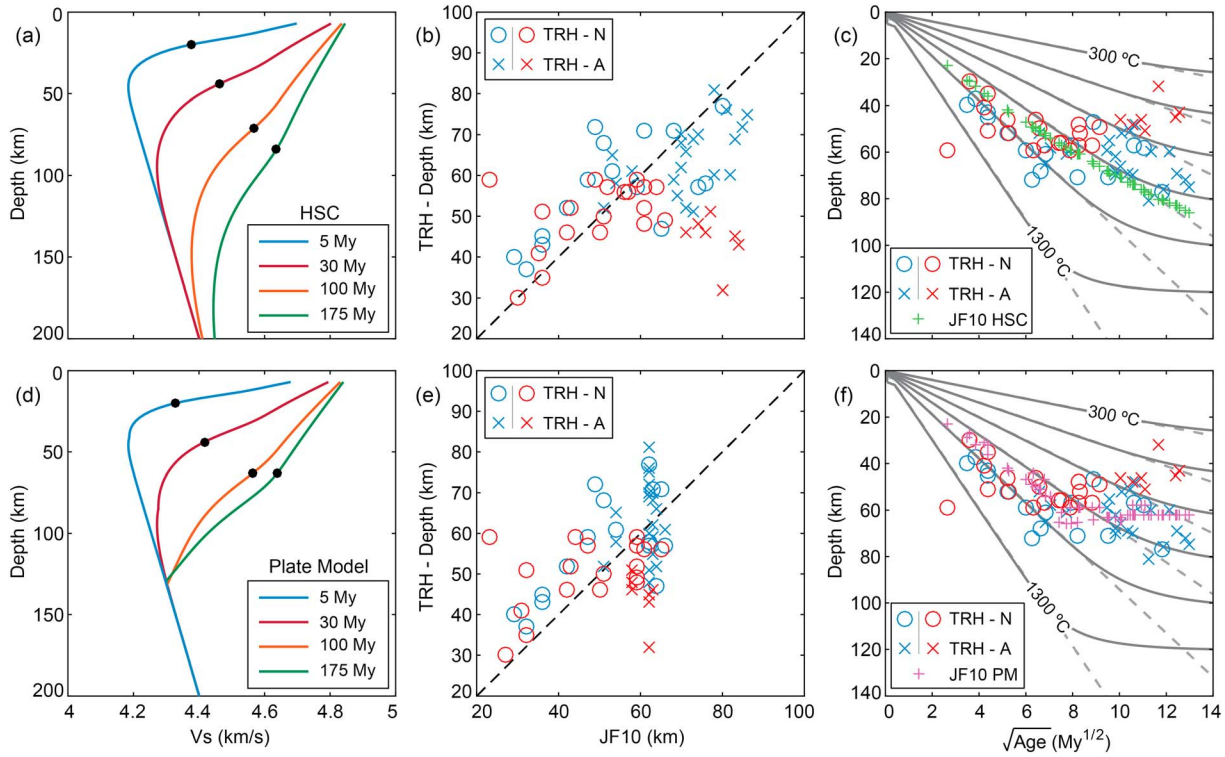

Figure 11. Our shallow pervasive discontinuity depths (TRH) compared to experimentally predicted depths for thermal models, JF10 [*Jackson and Faul*, 2010]. Predicted seismic velocities assuming grain size of 20 mm, appropriate for typical mantle temperatures of 1300–1450°C and water content of 50–2000 H/10^{6}Si at 150 km depth [*Behn et al*., 2009] for (a) half-space cooling (HSC) and (d) plate model (PM) [*Stein and Stein*, 1992]. TRH discontinuity depths compared to predicted depths from (b) HSC and (e) PM. Predicted depth is the center of the negative velocity gradient in both HSC and PM indicated by black markers in Figures 11a and 11b. TRH discontinuity and predicted depths compared with age of bins for (c) HSC and (f) PM. The circles and crosses correspond to normal (TRH-N) and anomalous lithosphere (TRH-A), respectively. The blue color shows results of single discontinuity, and the red color shows results of shallow discontinuity in bins with double negative discontinuity.

as the midpoint of the negative gradient in shear velocity for JF10, although the depth of the sharpest negative JF10 gradient is very similar (Figure 11). Our results for the shallow discontinuity are similar in depth range ($<\pm$10 km) to those estimated from JF10 for seafloor $<$36 Myr. For seafloor $>$36 Myr, our results are shallower than estimated from JF10 (Figures 11b and 11e). There is strong correlation, 0.81 for HSC and 0.81 for PM, between our results and estimations from JF10 for seafloor $<$36 Myr. However, our gradients are much sharper at all ages (3–15% over $<$21 km) compared to those predicted by JF10, 8–11.5% over $<$170 km for HSC, and 10–11.5% over $<$130 km for PM) (Figures 12 and 13). The magnitude of discontinuity sharpness (% change in velocity/total depth range) we model is on an average 4 times greater than the predictions from JF10 (Figure 12). The sharpness of the discontinuity and the lack of relationship between discontinuity depth and square root of age in comparison to the predictions from JF10 suggest that the discontinuity we image may not have a purely thermal origin, and other processes may be required to explain the discontinuity.

4.2.4. Mechanisms for the Shallow, Pervasive, Negative Discontinuity

4.2.4.1. Anisotropy

An abrupt change in seismic anisotropy could explain apparent velocity discontinuities in *SS* waveforms [*Rychert et al*., 2014b]. Azimuthal anisotropy would cause *SS* precursor underside reflections of varying amplitude and sign (positive or negative) depending on the back azimuth direction. Limitations in back azimuthal distribution of the data make tight constraints difficult. However, we attempted to detect polarity variations in the discontinuity required by our *SS* waveforms when stacked along different back azimuth ranges. Although we detect variations in amplitude with back azimuth, we do not see evidence for variations in polarity. In addition, we do not detect positive polarity discontinuities near ~60 km depth in any bins across the Pacific. This suggests that azimuthal anisotropy is not the only factor defining the observed discontinuity.

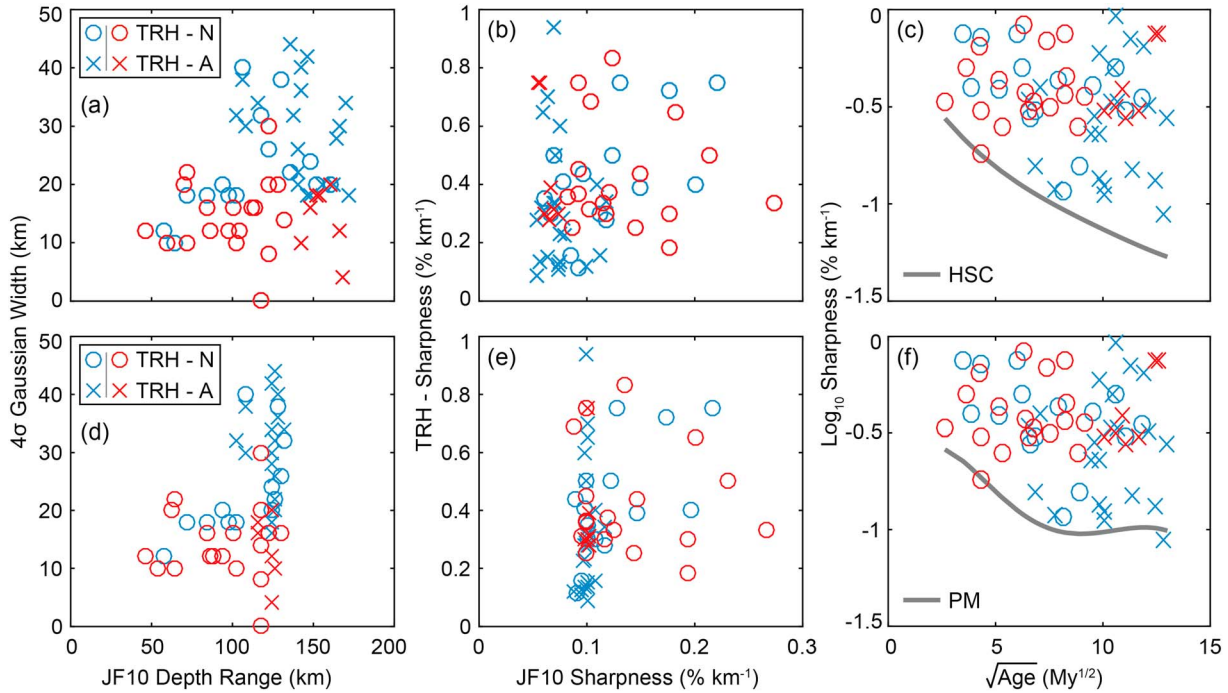

Figure 12. Discontinuity sharpness compared to predictions from thermal model. TRH refers to the present study. Gaussian width, i.e., $\pm 2\sigma$, of the discontinuity compared to total depth range of negative velocity gradient in JF10 for (a) HSC and (d) PM. TRH discontinuity sharpness, i.e., % change in velocity over total depth range, compared to JF10 discontinuity sharpness for (b) HSC and (e) PM. Logarithm of discontinuity sharpness (Log_{10} Sharpness) compared to seafloor age for (c) HSC and (f) PM. The solid grey line in Figures 12c and 12f shows sharpness estimates from JF10. The circles and crosses correspond to normal (TRH-N) and anomalous lithosphere (TRH-A) respectively. The blue color shows results of single discontinuity, and the red color shows results of shallow discontinuity in bins with double negative discontinuity.

Negative *SS* precursors could result from a sharp increase in radial anisotropy with depth. However, whether or not radial anisotropy is strongly increasing at 60 km depth is debated. An increase in radial anisotropy from 0 to 100 or 150 km depth is a feature of most global models [*Auer et al*., 2015; *Beghein et al*., 2014; *Burgos et al*., 2014; *Nettles and Dziewonski*, 2008]. Although, in situ regional constraints suggest that the strongest anisotropy is shallow [*Lin et al*., 2016; *Takeo et al*., 2013; *Weeraratne et al*., 2007]. These studies constrain azimuthal anisotropy that would translate to radial anisotropy if caused by horizontal alignment of olivine. In addition, if our results represent the same feature(s) imaged by receiver functions from the Pacific [*Kawakatsu et al*., 2009; *Kumar and Kawakatsu*, 2011], radial anisotropy cannot provide a simultaneous explanation [*Harmon et al*., 2016].

4.2.4.2. Compositional Boundary

Extraction of basaltic melt at a mid-ocean ridge may result in a dry, depleted residuum [*Hirth and Kohlstedt*, 1996]. The difference in seismic velocity between the seismically fast residuum and the slower deeper mantle beneath could produce a seismic velocity discontinuity, related to the depth of melting near ~60 km depth, which would be age-independent [*Gaherty et al*., 1999]. This resembles the depth of our results (50–80 km, average depth of ~60 km) beneath seafloor >36 Myr old which show no age dependence. Compositional boundaries can also be quite sharp [*Hirth and Kohlstedt*, 1996; *Rychert et al*., 2005; *Rychert et al*., 2007], certainly sufficient to explain our constraints on the depth range over which the discontinuity occurs. In terms of magnitude, typically chemical depletion can explain ~1% velocity contrast [*Schutt and Lesher*, 2006]. However, in the special situation where there is frozen-in melt at shallow depths as a garnet-rich rock like eclogite, the contrast could be larger, ~5% [*Hacker and Abers*, 2004]. In addition, although we parameterized the inversion in terms of seismic velocity, density effects from composition might also play a role, potentially enhancing the apparent contrast by 2–3%. Therefore, if a somewhat exotic melt composition is pervasively frozen-in to the lithosphere this could explain up to an ~8 % sharp contrast, satisfying the bulk of our observations beneath seafloor >36 Myr.

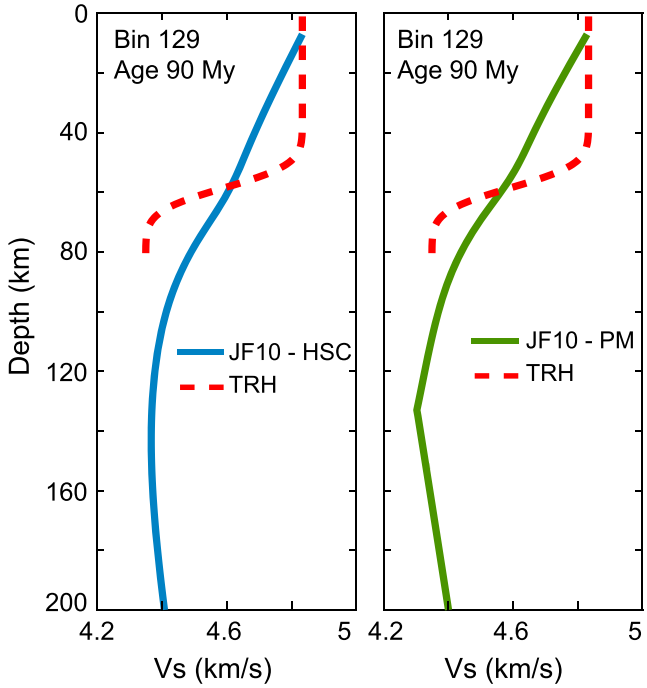

Figure 13. TRH velocity model for bin 129 with seafloor age of 90 Myr compared to JF10 velocity model for HSC (blue) and PM (green). Depth is in relation to seafloor.

Although dehydration may also contribute to seismic velocity discontinuities, it may not be significant beneath the older seafloor (>36 Myr) if the effect of hydrated olivine on seismic waves is diminished at cold temperatures [*Behn et al.*, 2009]. However, alternatively, it has been suggested that elastically accommodated grain boundary sliding could enhance the effect of water on seismic waves [*Karato et al.*, 2015; *Olugboji et al.*, 2013], and the temperature-pressure dependence of the effect would create a discontinuity with a similar age-depth dependence to our observations at younger ages. However, the magnitude of this effect is debated [*Jackson and Faul*, 2010] and experimental work on hydration is beginning to emerge [*Aizawa et al.*, 2008].

4.2.4.3. Partial Melt

The presence of melt in the asthenosphere could explain a large velocity drop with depth. This might occur along the solidus if melt is present in significant amounts just deeper than the solidus. At the mid-ocean ridge axis, large volumes of melt in the mantle (~1%) could produce a velocity drop of up to 7.9%, although the exact magnitude depends on the amount of melt and melt-distribution geometry [*Hammond and Humphreys*, 2000; *Kawakatsu et al.*, 2009]. Just off the ridge axis, the small degrees of asthenospheric melt could accumulate in regions where the solidus acts as a permeability boundary [*Hirschmann*, 2010; *Katz*, 2010; *Sparks and Parmentier*, 1991], enhancing the velocity contrast along the solidus out to ~40 Myr assuming 500 ppm water content [*Katz et al.*, 2003] (Figure 14). The melt concentration may be significantly higher at the permeability boundary (porosity on the order of 0.10 or 10% by volume) [*Sparks and Parmentier*, 1991]. At young seafloor ages (<36 Myr), the solidus happens to also be quite similar to the 1100°C isotherm and could explain the correlation at young ages (Figures 8 and 14). The enriched solidus (500 ppm water) diverges from the 1100°C isotherm at greater ages, although our resolution of the breakpoint does not allow us to distinguish between the two (Figure 8).

Beneath older seafloor, mantle melt production is expected to be small. In addition, temperatures are expected to be below the silicate melt solidus at 60 km depth. Volatiles such as water and CO_2 could enhance and stabilize a small degree of partial melt in the asthenosphere, although suboceanic mantle is expected to be depleted in volatiles, with correspondingly small melt contents (≪0.1% melt), insufficient to explain our result [*Hirschmann*, 2010]. In areas of local enrichment (~500 ppm H_2O and CO_2),

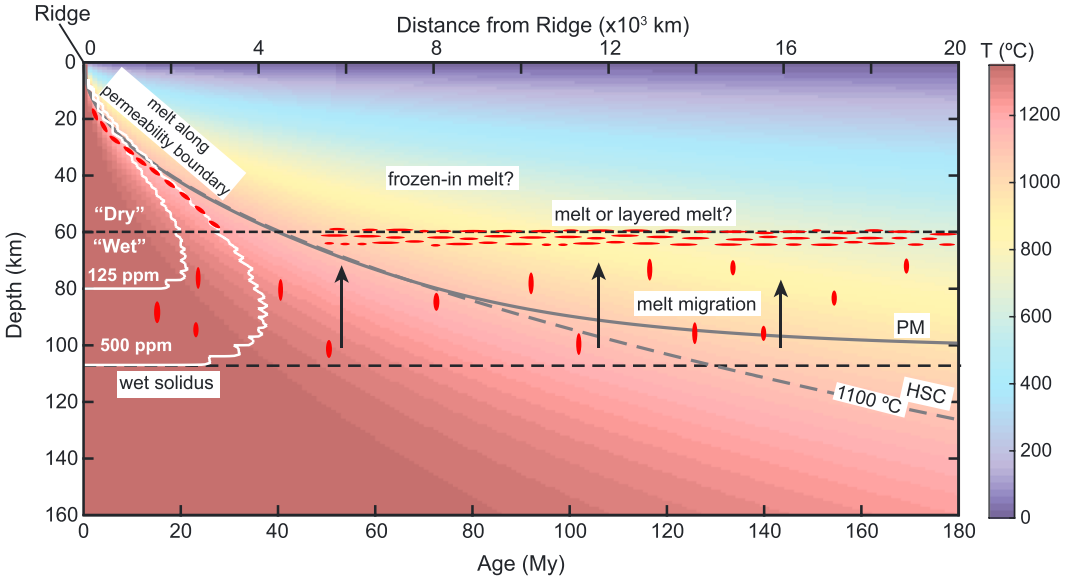

Figure 14. Schematic of a model that explain the shallow, sharp, pervasive negative discontinuity in our results. The solid and dashed grey lines show 1100°C isotherm for PM and HSC, respectively. The white lines show melt contours for a mantle melting model with varying amounts of water (ppm) [*Katz et al.*, 2003].

such as mantle plumes or subducting slabs, volatiles could potentially stabilize melt accumulation at 50–80 km depth to 140 Myr seafloor [*Sifre et al.*, 2014] through the formation of a permeability boundary and/or the neutral buoyancy of the melt [*Sakamaki et al.*, 2013]. Diking of asthenospheric melt and subsequent heating and thinning of the lithosphere [*Havlin et al.*, 2013] could explain an ~60 km lithosphere in regions with high melt production (at least 0.63% melt). However, all of these models require large, constant supply of volatiles and/or melt, which is not predicted over the entire Pacific. One possibility is that low degrees of asthenospheric carbonatite melt [*Hirschmann*, 2010] in horizontal bands such as suggested in the "millefeuille model" could produce the required velocity contrasts over large swaths of the Pacific without the need for extreme volatile and/or melt contents [*Kawakatsu et al.*, 2009], potentially explaining our observation. The melt would likely affect the strength of the mantle [*Faul*, 1997; *Hirth and Kohlstedt*, 1995], and the boundary would necessarily represent the lithosphere-asthenosphere boundary in this case [*Rychert et al.*, 2005; *Rychert et al.*, 2007; *Rychert and Shearer*, 2009].

5. Conclusions

We resolve a sharp, pervasive seismic discontinuity across the Pacific at 30–80 km depth with a 3–15% shear velocity drop over $<$21 km in depth. It increases in depth with age from the ridge to 36 ± 9 Myr according to conductive cooling along the 1100°C isotherm. Beneath older seafloor, $>$36 Myr, there is no apparent age-depth dependence and the discontinuity is imaged at a mean depth of 60 ± 1.5 km. A purely thermal origin of the discontinuity is unlikely as the velocity contrast is sharper than expected from thermal models. The discontinuity beneath younger seafloor is likely related to the accumulation of melt at a permeability boundary, which is controlled by the solidus depth. The discontinuity beneath older seafloor could be explained by a compositional boundary from a strong pervasive frozen-in melt signature. Although not necessarily the LAB, this type of pervasive compositional variation would probably influence mantle rheology and the LAB transition. Alternatively, melt could explain our observations at older ages where thin layers of carbonatitic melt form as in the "millefeuille" model and/or coalesces at a permeability boundary. In this situation the melt would likely weaken the mantle, and the boundary would then represent the LAB. An intermittent 4% drop in shear velocity over $<$11 km is imaged in the depth range of 80–120 km depth (average depth of ~100 km) with no apparent age dependence. In many cases, it could represent continually decreasing velocity in concert with the shallower feature.

Acknowledgments
We thank the reviewers for their insightful comments that have significantly improved the discussion presented in this paper. The global data set used for this study is available online at the Incorporated Research Institutions for Seismology (IRIS) data management center. This work is supported in part by Natural Environment Research Council grants NE/K000985/1 and NE/M003507/1.

References

Aizawa, Y., A. Barnhoorn, U. H. Faul, J. D. Fitz Gerald, I. Jackson, and I. Kovacs (2008), Seismic properties of Anita Bay Dunite: An exploratory study of the influence of water, *J. Petrol.*, *49*(4), 841–855, doi:10.1093/petrology/egn007.

Aki, K., and P. G. Richards (2009), *Quantative Seismology*, 2nd ed., pp. 700, Univ. Science Books, Calif.

Artemieva, I. M. (2006), Global 1 degrees × 1 degrees thermal model TC1 for the continental lithosphere: Implications for lithosphere secular evolution, *Tectonophysics*, *416*(1–4), 245–277, doi:10.1016/j.tecto.2005.11.022.

Auer, L., T. W. Becker, L. Boschi, and N. Schmerr (2015), Thermal structure, radial anisotropy, and dynamics of oceanic boundary layers, *Geophys. Res. Lett.*, *42*, 9740–9749, doi:10.1002/2015GL066246.

Bagley, B., and J. Revenaugh (2008), Upper mantle seismic shear discontinuities of the Pacific, *J. Geophys. Res.*, *113*, B12301, doi:10.1029/2008JB005692.

Barrell, J. (1914), The strength of the Earth's crust, *J. Geol.*, *22*(6), 537–555.

Beghein, C., K. Q. Yuan, N. Schmerr, and Z. Xing (2014), Changes in seismic anisotropy shed light on the nature of the Gutenberg discontinuity, *Science*, *343*(6176), 1237–1240, doi:10.1126/science.1246724.

Behn, M. D., G. Hirth, and J. R. Elsenbeck (2009), Implications of grain size evolution on the seismic structure of the oceanic upper mantle, *Earth Planet. Sci. Lett.*, *282*(1–4), 178–189, doi:10.1016/j.epsl.2009.03.014.

Bhattacharyya, J., G. Masters, and P. Shearer (1996), Global lateral variations of shear wave attenuation in the upper mantle, *J. Geophys. Res.*, *101*(B10), 22,273–22,289, doi:10.1029/96JB01782.

Bird, P. (2003), An updated digital model of plate boundaries, *Geochem. Geophys. Geosyst.*, *4*(3), 1027, doi:10.1029/2001GC000252.

Burgos, G., J. P. Montagner, E. Beucler, Y. Capdeville, A. Mocquet, and M. Drilleau (2014), Oceanic lithosphere-asthenosphere boundary from surface wave dispersion data, *J. Geophys. Res. Solid Earth*, *119*, 1079–1093, doi:10.1002/2013JB010528.

Chambers, K., A. Deuss, and J. H. Woodhouse (2005), Reflectivity of the 410-km discontinuity from PP and SS precursors, *J. Geophys. Res.*, *110*, B02301, doi:10.1029/2004JB003345.

Dalton, C. A., G. Ekstrom, and A. M. Dziewonski (2008), The global attenuation structure of the upper mantle, *J. Geophys. Res.*, *113*, B09303, doi:10.1029/2007JB005429.

Daly, R. A. (1940), Strength and structure of the Earth ix p., 1 ℓ., 434 p. incl. illus. (maps, charts) tables, diagrs, Prentice-Hall, New York.

Davy, B., and R. Wood (1994), Gravity and magnetic modeling of the Hikurangi Plateau, *Mar. Geol.*, *118*(1–2), 139–151, doi:10.1016/0025-3227(94)90117-1.

Davy, B., K. Hoernle, and R. Werner (2008), Hikurangi Plateau: Crustal structure, rifted formation, and Gondwana subduction history, *Geochem. Geophys. Geosyst.*, *9*, Q07004, doi:10.1029/2007GC001855.

Deuss, A. (2009), Global observations of mantle discontinuities using SS and PP precursors, *Surv. Geophys.*, *30*(4-5), 301–326, doi:10.1007/s10712-009-9078-y.

Deuss, A., and Woodhouse, J. H. (2002), A systematic search for mantle discontinuities using SS-precursors, *Geophys. Res. Lett.*, *29*(8), 1249, doi:10.1029/2002GL014768.

Draper, N. R., and H. Smith (1998), *Applied Regression Analysis*, 3rd ed., John Wiley, New York.

Dumoulin, C., M. P. Doin, and L. Fleitout (2001), Numerical simulations of the cooling of an oceanic lithosphere above a convective mantle, *Phys. Earth Planet. Inter.*, *125*(1–4), 45–64, doi:10.1016/S0031-9201(01)00233-3.

Faul, U. H. (1997), Permeability of partially molten upper mantle rocks from experiments and percolation theory, *J. Geophys. Res.*, *102*(B5), 10,299–10,311, doi:10.1029/96JB03460.

Fischer, K. M., H. A. Ford, D. L. Abt, and C. A. Rychert (2010), The lithosphere-asthenosphere boundary, *Annu. Rev. Earth Planet. Sci.*, *38*(1), 551–575, doi:10.1146/Annurev-Earth-040809-152438.

Flanagan, M. P., and P. M. Shearer (1998), Topography on the 410-km seismic velocity discontinuity near subduction zones from stacking of sS, sP, and pP precursors, *J. Geophys. Res.*, *103*(B9), 21,165–21,182, doi:10.1029/98JB00595.

Forsyth, D. W. (1992), Geophysical constraints on mantle flow and melt generation beneath midocean ridges, *Geophys. Monogr. Ser.*, *71*, 1–65.

French, S., V. Lekic, and B. Romanowicz (2013), Waveform tomography reveals channeled flow at the base of the oceanic asthenosphere, *Science*, *342*(6155), 227–230, doi:10.1126/Science.1241514.

Gaherty, J. B., M. Kato, and T. H. Jordan (1999), Seismological structure of the upper mantle: A regional comparison of seismic layering, *Phys. Earth Planet. Inter.*, *110*(1–2), 21–41, doi:10.1016/S0031-9201(98)00132-0.

Gu, Y. J., and Dziewonski, A. M. (2002), Global variability of transition zone thickness, *J. Geophys. Res.*, *107*(B7), 2135, doi:10.1029/2001JB000489.

Gu, Y. J., S. C. Webb, A. Lerner-Lam, and J. B. Gaherty (2005), Upper mantle structure beneath the eastern Pacific Ocean ridges, *J. Geophys. Res.*, *110*, B06305, doi:10.1029/2004JB003381.

Hacker, B. R., and G. A. Abers (2004), Subduction factory 3: An Excel worksheet and macro for calculating the densities, seismic wave speeds, and H2O contents of minerals and rocks at pressure and temperature, *Geochem. Geophys. Geosyst.*, *5*, Q01005, doi:10.1029/2003GC000614.

Hammond, W. C., and E. D. Humphreys (2000), Upper mantle seismic wave velocity: Effects of realistic partial melt geometries, *J. Geophys. Res.*, *105*(B5), 10,975–10,986, doi:10.1029/2000JB900041.

Harmon, N., D. W. Forsyth, and D. S. Weeraratne (2009), Thickening of young Pacific lithosphere from high-resolution Rayleigh wave tomography: A test of the conductive cooling model, *Earth Planet. Sci. Lett.*, *278*(1–2), 96–106, doi:10.1016/j.epsl.2008.11.025.

Harmon, N., C. A. Rychert, and T. W. Becker (2016), Constraints on the radially anisotropic component of seismic discontinuities at 60–100 km depth, AGU Fall Meeting, edited, San Francisco, Calif.

Havlin, C., E. M. Parmentier, and G. Hirth (2013), Dike propagation driven by melt accumulation at the lithosphere-asthenosphere boundary, *Earth Planet. Sci. Lett.*, *376*, 20–28, doi:10.1016/j.epsl.2013.06.010.

Heit, B., X. Yuan, M. Bianchi, R. Kind, and J. Gossler (2010), Study of the lithospheric and upper-mantle discontinuities beneath eastern Asia by SS precursors, *Geophys. J. Int.*, *183*(1), 252–266, doi:10.1111/j.1365-246X.2010.04714.x.

Hirschmann, M. M. (2010), Partial melt in the oceanic low velocity zone, *Phys. Earth Planet. Inter.*, *179*(1–2), 60–71, doi:10.1016/J.Pepi.2009.12.003.

Hirth, G., and D. L. Kohlstedt (1995), Experimental constraints on the dynamics of the partially molten upper-mantle—Deformation in the diffusion creep regime, *J. Geophys. Res.*, *100*(B2), 1981–2001, doi:10.1029/94JB02128.

Hirth, G., and D. L. Kohlstedt (1996), Water in the oceanic upper mantle: Implications for rheology, melt extraction and the evolution of the lithosphere, *Earth Planet. Sci. Lett.*, *144*(1–2), 93–108, doi:10.1016/0012-821x(96)00154-9.

Hosmer, D. W., T. Hosmer, S. Le Cessie, and S. Lemeshow (1997), A comparison of goodness-of-fit tests for the logistic regression model, *Stat. Med.*, *16*(9), 965–980, doi:10.1002/(Sici)1097-0258(19970515)16:9<965:Aid-Sim509>3.3.Co;2-F.

Houser, C., G. Masters, M. Flanagan, and P. Shearer (2008), Determination and analysis of long-wavelength transition zone structure using SS precursors, *Geophys. J. Int.*, *174*(1), 178–194, doi:10.1111/j.1365-246X.2008.03719.x.
Huang, J. S., and S. J. Zhong (2005), Sublithospheric small-scale convection and its implications for the residual topography at old ocean basins and the plate model, *J. Geophys. Res.*, *110*, B05404, doi:10.1029/2004JB003153.
Jackson, I., and U. H. Faul (2010), Grainsize-sensitive viscoelastic relaxation in olivine: Towards a robust laboratory-based model for seismological application, *Phys. Earth Planet. Inter.*, *183*(1–2), 151–163, doi:10.1016/J.Pepi.2010.09.005.
Jones, A. G., I. J. Ferguson, A. D. Chave, R. L. Evans, and G. W. McNeice (2001), Electric lithosphere of the Slave craton, *Geology*, *29*(5), 423–426, doi:10.1130/0091-7613(2001)029<0423:Elotsc>2.0.Co;2.
Karato, S. I. (2012), On the origin of the asthenosphere, *Earth Planet. Sci. Lett.*, *321*, 95–103, doi:10.1016/j.epsl.2012.01.001.
Karato, S. I., T. Olugboji, and J. Park (2015), Mechanisms and geologic significance of the mid-lithosphere discontinuity in the continents, *Nat. Geosci.*, *8*(7), 509–514, doi:10.1038/Ngeo2462.
Katz, R. F. (2010), Porosity-driven convection and asymmetry beneath mid-ocean ridges, *Geochem. Geophys. Geosyst.*, *11*, Q0AC07, doi:10.1029/2010GC003282.
Katz, R. F., M. Spiegelman, and C. H. Langmuir (2003), A new parameterization of hydrous mantle melting, *Geochem. Geophys. Geosyst.*, *4*(9), 1073, doi:10.1029/2002GC000433.
Kawakatsu, H., P. Kumar, Y. Takei, M. Shinohara, T. Kanazawa, E. Araki, and K. Suyehiro (2009), Seismic evidence for sharp lithosphere-asthenosphere boundaries of oceanic plates, *Science*, *324*(5926), 499–502, doi:10.1126/science.1169499.
Korenaga, J. (2015), Seafloor topography and the thermal budget of Earth, *Geol. Soc. Am. Spec. Pap.*, *514*, 167–185.
Korenaga, T., and J. Korenaga (2008), Subsidence of normal oceanic lithosphere, apparent thermal expansivity, and seafloor flattening, *Earth Planet. Sci. Lett.*, *268*(1–2), 41–51, doi:10.1016/j.epsl.2007.12.022.
Kumar, P., and H. Kawakatsu (2011), Imaging the seismic lithosphere-asthenosphere boundary of the oceanic plate, *Geochem. Geophys. Geosyst.*, *12*, Q01006, doi:10.1029/2010GC003358.
Laske, G., G. Masters, Z. Ma, and M. Pasyanos (2012), CRUST1.0: An updated global model of Earth's crust European Geoscience Union, edited, Geophysical Research Abstracts, Vienna, Austria.
Lawrence, J. F., and P. M. Shearer (2008), Imaging mantle transition zone thickness with SdS-SS finite-frequency sensitivity kernels, *Geophys. J. Int.*, *174*(1), 143–158, doi:10.1111/j.1365-246X.2007.03673.x.
Lin, P.-Y. P., J. B. Gaherty, G. Jin, J. A. Collins, D. Lizarralde, R. L. Evans, and G. Hirth (2016), High-resolution seismic constraints on flow dynamics in the oceanic asthenosphere, *Nature*, doi:10.1038/nature18012.
Maggi, A., E. Debayle, K. Priestley, and G. Barruol (2006), Azimuthal anisotropy of the Pacific region, *Earth Planet. Sci. Lett.*, *250*(1–2), 53–71, doi:10.1016/J.Epsl.2006.07.010.
Moorkamp, M., A. G. Jones, and S. Fishwick (2010), Joint inversion of receiver functions, surface wave dispersion, and magnetotelluric data, *J. Geophys. Res.*, *115*, B04318, doi:10.1029/2009JB006369.
Müller, R. D., A. Dutkiewicz, M. Seton, and C. Gaina (2013), Seawater chemistry driven by supercontinent assembly, breakup, and dispersal, *Geology*, *41*(8), 907–910, doi:10.1130/G34405.1.
Nettles, M., and A. M. Dziewonski (2008), Radially anisotropic shear velocity structure of the upper mantle globally and beneath North America, *J. Geophys. Res.*, *113*, B02303, doi:10.1029/2006JB004819.
Nishimura, C. E., and D. W. Forsyth (1989), The anisotropic structure of the upper mantle in the Pacific, *Geophys. J. Int.*, *96*(2), 203–229, doi:10.1111/j.1365-246X.1989.tb04446.x.
Niu, F. L., S. C. Solomon, P. G. Silver, D. Suetsugu, and H. Inoue (2002), Mantle transition-zone structure beneath the South Pacific Superswell and evidence for a mantle plume underlying the Society hotspot, *Earth Planet. Sci. Lett.*, *198*(3–4), 371–380, doi:10.1016/S0012-821x(02)00523-X.
Olugboji, T. M., S. Karato, and J. Park (2013), Structures of the oceanic lithosphere-asthenosphere boundary: Mineral-physics modeling and seismological signatures, *Geochem. Geophys. Geosyst.*, *14*, 880–901, doi:10.1002/Ggge.20086.
Olugboji, T. M., J. Park, S.-I. Karato, and M. Shinohara (2016), Nature of the seismic lithosphere-asthenosphere boundary within normal oceanic mantle from high-resolution receiver functions, *Geochem. Geophys. Geosyst.*, *17*, 1265–1282, doi:10.1002/2015GC006214.
Parsons, B., and D. Mckenzie (1978), Mantle convection and thermal structure of plates, *J. Geophys. Res.*, *83*(Nb9), 4485–4496, doi:10.1029/JB083iB09p04485.
Parsons, B., and J. G. Sclater (1977), Analysis of variation of ocean-floor bathymetry and heat-flow with age, *J. Geophys. Res.*, *82*(5), 803–827, doi:10.1029/JB082i005p00803.
Price, K. V., R. M. Storn, and J. A. Lampinen (2005), *Differential Evolution: A Practical Approach to Global Optimization*, pp. 533, Springer, Berlin.
Regan, J., and D. L. Anderson (1984), Anisotropic models of the upper mantle, *Phys. Earth Planet. Inter.*, *35*(4), 227–263, doi:10.1016/0031-9201(84)90020-7.
Ritzwoller, M. H., N. M. Shapiro, and S. J. Zhong (2004), Cooling history of the Pacific lithosphere, *Earth Planet. Sci. Lett.*, *226*(1–2), 69–84, doi:10.1016/j.epsl.2004.07.032.
Rychert, C. A., and P. M. Shearer (2009), A global view of the lithosphere-asthenosphere boundary, *Science*, *324*(5926), 495–498, doi:10.1126/science.1169754.
Rychert, C. A., and P. M. Shearer (2010), Resolving crustal thickness using SS waveform stacks, *Geophys. J. Int.*, *180*(3), 1128–1137, doi:10.1111/j.1365-246X.2009.04497.x.
Rychert, C. A., and P. M. Shearer (2011), Imaging the lithosphere-asthenosphere boundary beneath the Pacific using SS waveform modeling, *J. Geophys. Res.*, *116*, B07307, doi:10.1029/2010JB008070.
Rychert, C. A., K. M. Fischer, and S. Rondenay (2005), A sharp lithosphere-asthenosphere boundary imaged beneath eastern North America, *Nature*, *436*(7050), 542–545, doi:10.1038/Nature03904.
Rychert, C. A., S. Rondenay, and K. M. Fischer (2007), P-to-S and S-to-P imaging of a sharp lithosphere-asthenosphere boundary beneath eastern North America, *J. Geophys. Res.*, *112*, B08314, doi:10.1029/2006JB004619.
Rychert, C. A., K. M. Fischer, G. A. Abers, T. Plank, E. Syracuse, J. M. Protti, V. Gonzalez, and W. Strauch (2008), Strong along-arc variations in attenuation in the mantle wedge beneath Costa Rica and Nicaragua, *Geochem. Geophys. Geosyst.*, *9*, Q10SD10, doi:10.1029/2008GC002040.
Rychert, C. A., N. Schmerr, and N. Harmon (2012), The Pacific lithosphere-asthenosphere boundary: Seismic imaging and anisotropic constraints from SS waveforms, *Geochem. Geophys. Geosyst.*, *13*, Q0AK10, doi:10.1029/2012GC004194.
Rychert, C. A., N. Harmon, and C. Ebinger (2014a), Receiver function imaging of lithospheric structure and the onset of melting beneath the Galapagos Archipelago, *Earth Planet. Sci. Lett.*, *388*, 156–165, doi:10.1016/J.Epsl.2013.11.027.
Rychert, C. A., N. Harmon, and N. Schmerr (2014b), Synthetic waveform modelling of SS precursors from anisotropic upper-mantle discontinuities, *Geophys. J. Int.*, *196*(3), 1694–1705, doi:10.1093/gji/ggt474.

Sakamaki, T., A. Suzuki, E. Ohtani, H. Terasaki, S. Urakawa, Y. Katayama, K. Funakoshi, Y. B. Wang, J. W. Hernlund, and M. D. Ballmer (2013), Ponded melt at the boundary between the lithosphere and asthenosphere, *Nat. Geosci.*, *6*(12), 1041–1044, doi:10.1038/Ngeo1982.

Schmerr, N. (2012), The Gutenberg discontinuity: Melt at the lithosphere-asthenosphere boundary, *Science*, *335*(6075), 1480–1483, doi:10.1126/science.1215433.

Schutt, D. L., and C. E. Lesher (2006), Effects of melt depletion on the density and seismic velocity of garnet and spinel lherzolite, *J. Geophys. Res.*, *111*, B05401, doi:10.1029/2003JB002950.

Shearer, P. M. (1991a), Constraints on upper mantle discontinuities from observations of long-period reflected and converted phases, *J. Geophys. Res.*, *96*(B11), 18,147–18,182, doi:10.1029/91JB01592.

Shearer, P. M. (1991b), Imaging global body wave phases by stacking long-period seismograms, *J. Geophys. Res.*, *96*(B12), 20,353–20,364, doi:10.1029/91JB00421.

Shearer, P. M. (1993), Global mapping of upper-mantle reflectors from long-period Ss precursors, *Geophys. J. Int.*, *115*(3), 878–904, doi:10.1111/j.1365-246X.1993.tb01499.x.

Shearer, P. M. (1996), Transition zone velocity gradients and the 520-km discontinuity, *J. Geophys. Res.*, *101*(B2), 3053–3066, doi:10.1029/95JB02812.

Shearer, P. M., and T. G. Masters (1992), Global mapping of topography on the 660-km discontinuity, *Nature*, *355*(6363), 791–796, doi:10.1038/355791a0.

Shearer, P. M., M. P. Flanagan, and M. A. H. Hedlin (1999), Experiments in migration processing of SS precursor data to image upper mantle discontinuity structure, *J. Geophys. Res.*, *104*(B4), 7229–7242, doi:10.1029/1998JB900119.

Sifre, D., E. Gardes, M. Massuyeau, L. Hashim, S. Hier-Majumder, and F. Gaillard (2014), Electrical conductivity during incipient melting in the oceanic low-velocity zone, *Nature*, *509*(7498), 81–85, doi:10.1038/nature13245.

Smith, W. H. F., and D. T. Sandwell (1997), Global sea floor topography from satellite altimetry and ship depth soundings, *Science*, *277*(5334), 1956–1962, doi:10.1126/science.277.5334.1956.

Sparks, D. W., and E. M. Parmentier (1991), Melt extraction from the mantle beneath spreading centers, *Earth Planet. Sci. Lett.*, *105*(4), 368–377, doi:10.1016/0012-821x(91)90178-K.

Stein, C. A., and S. Stein (1992), A model for the global variation in oceanic depth and heat-flow with lithospheric age, *Nature*, *359*(6391), 123–129, doi:10.1038/359123a0.

Storn, R., and K. Price (1997), Differential evolution—A simple and efficient heuristic for global optimization over continuous spaces, *J. Global Optim.*, *11*(4), 341–359, doi:10.1023/A:1008202821328.

Takeo, A., K. Nishida, T. Isse, H. Kawakatsu, H. Shiobara, H. Sugioka, and T. Kanazawa (2013), Radially anisotropic structure beneath the Shikoku Basin from broadband surface wave analysis of ocean bottom seismometer records, *J. Geophys. Res. Solid Earth*, *118*, 2878–2892, doi:10.1002/jgrb.50219.

Tan, Y., and D. V. Helmberger (2007), Trans-Pacific upper mantle shear velocity structure, *J. Geophys. Res.*, *112*, B08301, doi:10.1029/2006JB004853.

Taylor, B. (2006), The single largest oceanic plateau: Ontong Java-Manihiki-Hikurangi, *Earth Planet. Sci. Lett.*, *241*(3–4), 372–380, doi:10.1016/J.Epsl.2005.11.049.

Tharimena, S., C. A. Rychert, and N. Harmon (2016), Seismic imaging of a mid-lithospheric discontinuity beneath Ontong Java Plateau, *Earth Planet. Sci. Lett.*, *450*, 62–70, doi:10.1016/j.epsl.2016.06.026.

Watts, A. B. (1978), Analysis of isostasy in the worlds oceans 1. Hawaiian-Emperor Seamount Chain, *J. Geophys. Res.*, *83*(Nb12), 5989–6004, doi:10.1029/JB083iB12p05989.

Weeraratne, D. S., D. W. Forsyth, Y. Yang, and S. C. Webb (2007), Rayleigh wave tomography beneath intraplate volcanic ridges in the South Pacific, *J. Geophys. Res.*, *112*, B06303, doi:10.1029/2006JB004403.